

# Understanding Pan-Sharpening via Generalized Inverse

Shiqi Liu, Yihua Tan, Yutong Bai, Alan Yuille

**Abstract**—Pan-sharpening algorithms utilize a panchromatic image and a multispectral image to generate a high spatial and high spectral image. However, the optimizations of the algorithms are designed with different standards. We employ a simple matrix equation to describe the Pan-sharpening problem. The conditions for the existence of a solution and the acquisition of spectral and spatial resolution are discussed. A down-sampling enhancement method is introduced to improve the estimation of spatial and spectral down-sample matrices.

Using generalized inverse theory, we discovered two kinds of solution spaces of generalized inverse matrix formulations, which correspond to the two prominent classes of Pan-sharpening methods: component substitution and multi-resolution analysis. Specifically, the Gram-Schmidt adaptive method is demonstrated to align with the generalized inverse matrix formulation of component substitution. A model prior of the generalized inverse matrix of the spectral function is rendered. Theoretical errors are analyzed. The diffusion prior is naturally embedded with the help of general solution spaces of the generalized inverse form, enabling the acquisition of refined Pan-sharpening results.

Extensive experiments, including comparative, synthetic, real-data ablation and diffusion-related tests are conducted. The proposed methods produce qualitatively sharper and superior results in both synthetic and real experiments. The down-sampling enhancement method demonstrates quantitatively and qualitatively better outcomes in real-data experiments. The diffusion prior can significantly improve the performance of our methods across almost all evaluation measures.

The generalized inverse matrix theory helps deepen the understanding of Pan-sharpening mechanisms.

**Index Terms**—Pan-sharpening, Generalized Inverse, Image Fusion, Hyperspectral Processing, Matrix Theory, Diffusion Model.

## I. INTRODUCTION

Surpassing 70% of optical observation satellites are equipped with low-resolution multispectral (MS) and high-resolution panchromatic (PAN) sensors [1]. Although high-resolution multispectral sensors can capture clear and colorful images, most optical observation satellites do not adopt this sensor. This situation is attributed to following scientific limitations.

Shiqi Liu and Yihua Tan are with Huazhong University of Science and Technology, Wuhan, 430074, Hubei, China(e-mail: shiqi.liu647@foxmail.com; yhtan@hust.edu.cn).

Yutong Bai is with University of California, Berkeley, Berkeley, 94720, California, United States(e-mail: ytongbai@gmail.com).

Alan Yuille is with Johns Hopkins University, Baltimore, 21218, Maryland, United States.(e-mail: ayuille1@jhu.edu).

The prototype for this work was developed during an internship at the CCVL lab at Johns Hopkins University. It was later improved and finalized in Yihua Tan's laboratory at Huazhong University of Science and Technology.

Yihua Tan is the corresponding author.

- Energy limitation [1]: The energy per unit area emitted into the optical sensor is limited, while the sensing capability of the sensor per unit is also restricted. The energy per unit area utilizes multiple optical sensors to receive; each sensor receives a portion of the energy. If several smaller sensors are tiled, each sensor receives the corresponding energy. This energy requires a sensor with a stronger sensing ability. Therefore, the energy emitted into the sensor must be negotiated with the sensing ability of the sensor.
- On-board storage and data transmission rate limitations [1]: The storage capacity of satellites is limited. Besides, the transmission velocity between the satellite and receiver platform is also limited. As a result, the use of high-resolution MS sensors means that higher transmission speeds are required.

To enhance vision performance using collected images from multispectral and panchromatic sensors, various image fusion methods have been proposed. Most of these methods can generally be classified into multi-resolution analysis and component substitution techniques [2].

Multi-Resolution Analysis (MRA) methods, also known as spatial methods, decompose the PAN image into multiple scales to extract its spatial information. Common decomposition techniques used in Pan-sharpening include Laplacian pyramids, wavelets, curvelets, and contourlets. MRA-based fusion offers advantages such as maintaining temporal coherence and spectral consistency, and is robust to aliasing, making it a promising area for future research. In regard to multi-resolution analysis(MRA), there are following methods

- High pass filtering methods [3]: Firstly, they extract the high-frequency part of the PAN image. Then, they consider the variance proportion of the valid image pixel value of the MS and PAN as the weight. Next, they add the weighted high-frequency part to the up-sampled multispectral image and finally achieve Pan-sharpening. While these methods represent an interesting trial, the measurement quantity of the high-frequency part of the PAN image is not transformed to the measurement quantity of the MS image. Consequently, the fusion performance, affected by the PAN image pixel scale, could be excessively blurred or sharp.
- Wavelet transformation methods [4]: They utilize wavelet transformation to extract different frequency components for fusion.
- MTF-GLP-HPM-R methods [5]: They use a Generalized Laplacian Pyramid (GLP) with filters that match

the Modulation Transfer Function (MTF) and high-pass modulation injection. This method also includes an initial step of spectral matching based on regression analysis.

- MTF-GLP-CBD methods [6]: They first extract the high-frequency component of the PAN image. Then, they use the quotient of the covariance between the low-resolution PAN and MS and the variance of low-resolution PAN to weight the high-frequency component. Finally, they add the weighted high-frequency component to the upsampled MS image to obtain the result.
- MTF-GLP-FS methods [7]: They address the estimation of full-resolution injection coefficients for regression-based Pan-sharpening. Specifically, they focus on the effective GLP method using MTF-matched filter regression. They propose and analyze an iterative algorithm that estimates these coefficients at full scale.

Component substitution (CS) methods, also known as spectral methods, enhance the spatial detail of MS images by projecting them into a different domain. This transformation separates the spatial information, which is then replaced with the high-resolution detail from a PAN image. Due to their straightforward implementation, CS techniques have been widely used in Pan-sharpening, with early examples including intensity-hue-saturation (IHS) and principal component analysis (PCA) methods from the 1990s. Regarding CS methods, there are following methods,

- IHS methods [8]: They first extract the intensity, hue, saturation bands from the MS image. Then, they utilize high resolution PAN image to replace the intensity band. Finally, they reconstruct the image. The fusion number of band is limited to three.
- PCA methods [9]: First, they perform principal component decomposition of a MS image. Then, they replace the first principal component with the PAN image. Finally, they apply an inverse transformation to reconstruct the high resolution image. However, these novel methods are limited by spectral and spatial inconsistencies, which may alter the spectral properties.
- Gram schmidt adaptive(GSA) methods [10], [11]: They first synthesize PAN by using the upsampled projected MS image. Then, they calculate the difference between the synthetic PAN and the original PAN. They use adaptive parameters to up-recover the difference value in different spectral channels. Finally, they add the up-recovered value to the spatial up-sampled multi-spectral image to obtain the high spatial and spectral resolution results.
- C-GSA [12]: They determine the weights for injecting spatial detail from a PAN image into MS channels by proposing a novel, context-adaptive (local) method for estimating these injection coefficients, based on image segmentation. They assign region-specific coefficients, ensuring that all pixels within a segmented region share the same weights, while allowing for variations between regions. A Binary Partition Tree segmentation, applied to the MS image, generates the regions used for coefficient calculation.

- BT-H [13]: They use the optimized Brovey transform [14] and include haze correction [13].
- BDSD-PC [15]: They extract spatial details that vary by band in Pan-sharpening while incorporating physical constraints.

Other methods, including variational optimization methods and deep learning methods, have also been proposed to solve the Pan-sharpening problem.

Variational Optimization (VO) methods, which solve optimization models, have gained significant popularity due to advancements in convex optimization and inverse problems. These methods have been successfully applied in areas such as MS Pan-sharpening and hyperspectral (HS) image fusion. VO approaches typically establish a model based on the relationship between the input PAN image, the low-resolution MS image, and the desired high-resolution MS image. However, the underlying problem is inherently ill-posed, necessitating the use of regularizers that incorporate prior knowledge about the desired high-resolution MS image to constrain the solution space. The typical methods including SR-D [16] and TV [17].

Deep learning (DL) techniques have become prevalent in MS Pan-sharpening and HS image fusion. The first DL-based Pan-sharpening approach, [18], adapted an autoencoder inspired by sparse denoising. In 2016, [19] introduced the first fully convolutional neural network (CNN) for Pan-sharpening, termed the Pan-sharpening neural network (PNN), which used a three-layer architecture inspired by a super-resolution CNN. Also in 2016, [20] proposed a compressed sensing Pan-sharpening method using the Gram-Schmidt transform and a pre-existing super-resolution CNN. These initial studies spurred significant research interest in DL-based Pan-sharpening, leading to numerous publications. Deep learning methods [21], [22], [23], [24], [25], [26], [27], [28], [29], [30], [31], [32], [33] incorporate more prior knowledge for Pan-sharpening tasks. Consequently, current research focuses on developing novel network architectures and pre-processing techniques to enhance generalization.

There are numerous mathematical deduction of different CS and MRA methods [2] [34]. However, the implicit objectives of different CS and MRA methods were not fully optimized and still lacked exploration. What kind of mathematical models do CS and MRA methods solve, and what are their solution spaces? How to perform refined optimization in the solution space to obtain a better solution? These questions need to be explored and answered.

In this paper, based on the matrix equations of the Pan-sharpening problem, we discover two kinds of solution spaces regarding the generalized inverse solution expression. According to the generalized inverse representation, we find that these two solution spaces correspond to the general CS class of methods and the general MRA class of methods. Choosing different generalized inverse matrices yields different methods. Furthermore, it yields down-sampling enhancement for better fusion results. We show that the GSA method corresponds precisely to the generalized inverse expression of CS methods. We then embed prior knowledge in the range of the generalized inverse of the spectral response matrix. We analyze the errors in different cases. Additionally, we demonstrate

that if the down-sampling enhancement is implemented, then CS methods and MRA methods produce the same results. To further incorporate the prior knowledge of the diffusion model, we substitute the general solution spaces of the generalized inverse form into the evidence lower bound of the diffusion model and optimize the auxiliary matrix to obtain a refined Pan-sharpening solution. Based on the matrix representation, we propose five different evaluation indicators. Both synthetic and real data experiments show that the results align with generalized inverse theory and that our method, incorporating prior and down-sampling enhancement, yields sharper qualitative results. The experiment conducted to validate the effect of the diffusion prior demonstrates that the diffusion prior can significantly improve the performance of our methods across almost all evaluation measures.

The main contributions are as follows:

- **The integration of generalized inverse theory with CS and MRA methods yields two general solution spaces, bridging the gap between mathematical theory and Pan-sharpening techniques.** This integration helps clarify the implicit objectives of different CS and MRA methods that were previously not fully explored. It provides a unified mathematical framework to understand how these two prominent classes of Pan-sharpening methods operate. By establishing this connection, it enables a deeper exploration of the solution spaces for further optimization.
- **We derive the precise correspondence between GSA methods and the generalized inverse representation of CS methods.** This correspondence shows that GSA is a special case within the CS framework's generalized inverse representation, enhancing the understanding of GSA's mathematical foundation and its relationship with broader CS methods. It allows GSA to be further refined and optimized using potential prior knowledge, such as diffusion priors.
- **We improve the estimation of spatial and spectral response matrices using down-sampling enhancement.** Experiments demonstrate that this enhancement results in better quantitative and qualitative outcomes for both CS and MRA methods.
- **Embedding prior knowledge in the range of the generalized inverse of the spectral response matrix helps obtain sharper reconstructed images.** Empirically, it is found that when elements of the generalized inverse are close to 1, the image is sharper, while smaller elements cause blurring. By restricting the generalized inverse's elements to a range around 1 (0.9-1.4), the method avoids blurred features.
- **Incorporating diffusion model prior knowledge into the generalized inverse solution spaces leads to refined Pan-sharpening results.** The general solution spaces of the generalized inverse form are substituted into the evidence lower bound of the diffusion model, and the auxiliary matrix is optimized using Score Distillation Sampling. Experiments validate that the diffusion prior significantly improves performance across almost all eval-

uation measures. This integration leverages the diffusion model's prior knowledge to further refine solutions within the general solution spaces.

In the following sections, we denote the scalar, vector, matrix, and corresponding random variable in the non-bold case, bold case, bold upper case, respectively.

## II. METHODOLOGY

Suppose the desired high spatial resolution and high spectral resolution (HrHS) is  $\mathbf{X}$ , and we have high spatial resolution low spectral resolution (HrLS)  $\mathbf{Y}$  and low spatial resolution and high spectral resolution (LrHS)  $\mathbf{Z}$ . We can express their relationship using the following model.

### A. Model

**Assumption II.1.**  $\mathbf{X} \in R^{HW \times S}$  is HrHS,  $\mathbf{Y} \in R^{HW \times s}$  is HrLS,  $\mathbf{Z} \in R^{hw \times S}$  is LrHS.

$$\mathbf{Y} = \mathbf{XA} \quad (1)$$

$$\mathbf{Z} = \mathbf{BX} \quad (2)$$

where  $\mathbf{A} \in R^{S \times s}$  is the spectral response function,  $\mathbf{B} \in R^{hw \times HW}$  is the spatial response function, respectively.

$H$  is the height of high spatial resolution images,  $W$  is the width of high spatial resolution images,  $h$  is the height of low spatial resolution images,  $w$  is the width of low spatial resolution images,  $S$  is the spectral number of high spectral images and  $s$  is the spectral number of low spectral images. We mainly focus on the case where  $s = 1$ .

This model demonstrates that we can regard the HrLS  $\mathbf{Y}$  and LrHS  $\mathbf{Z}$  as projections of HrHS  $\mathbf{X}$  on different sides, determined by the spectral response function  $\mathbf{A}$  and the spatial response function  $\mathbf{B}$ , respectively. We also refer to  $\mathbf{B}$  as the spatial down-sampling matrix and to  $\mathbf{A}$  as the spectral down-sampling matrix.

### B. Definition of Generalized Inverse

In order to introduce the solution for the model II.1, we first present the definition of the generalized inverse.

**Definition II.2.** [35]  $\mathbf{A}^-$  is the generalized inverse of a matrix  $\mathbf{A}$  if  $\mathbf{AA}^- \mathbf{A} = \mathbf{A}$ . We define  $\mathbf{A}\{-\} = \{\mathbf{A}^- | \mathbf{AA}^- \mathbf{A} = \mathbf{A}\}$  to be the set of all the generalized inverse of  $\mathbf{A}$ .

Further, if  $\mathbf{A}^- \mathbf{AA}^- = \mathbf{A}^-$ ,  $(\mathbf{A}^- \mathbf{A})^T = \mathbf{A}^- \mathbf{A}$  and  $(\mathbf{AA}^-)^T = \mathbf{AA}^-$  then we define this  $\mathbf{A}^-$  as the Moore-Penrose inverse and denote it as  $\mathbf{A}^+$ .

We can see that the generalized inverse inherits one property  $\mathbf{AA}^- \mathbf{A} = \mathbf{A}$  of the normal inverse.

### C. Properties

**Theorem II.3.** [36], the matrix equations in Assumption II.1 have a solution if and only if

$$\mathbf{BY} = \mathbf{ZA} \quad (3)$$

$$\mathbf{Y} = \mathbf{YA}^- \mathbf{A} \quad (4)$$

$$\mathbf{Z} = \mathbf{BB}^- \mathbf{Z}. \quad (5)$$

where  $\mathbf{A}^-$  refers to any generalized inverse of matrix  $\mathbf{A}$ , and  $\mathbf{B}^-$  refers to any generalized inverse of matrix  $\mathbf{B}$ .

This theorem uses generalized inverses to establish the existence condition for the solution to the model.

#### D. Solution for $\mathbf{A}$ and $\mathbf{B}$

**Theorem II.4.** *We can use linear equations to rewrite the  $\mathbf{BY} - \mathbf{ZA}$  in Kronecker form, i.e,*

$$[\mathbf{Z}_{hw \times S} \otimes \mathbf{I}_{s \times s}, -\mathbf{I}_{hw \times hw} \otimes \mathbf{Y}_{s \times HW}^T] \begin{bmatrix} \text{vec}(\mathbf{A}) \\ \text{vec}(\mathbf{B}) \end{bmatrix}_{Ss + hwHW} = 0 \quad (6)$$

where the Kronecker product  $\mathbf{Z} \otimes \mathbf{I} = \begin{bmatrix} z_{1,1}\mathbf{I} & z_{1,2}\mathbf{I} & \cdots & z_{1,S}\mathbf{I} \\ z_{2,1}\mathbf{I} & z_{2,2}\mathbf{I} & \cdots & z_{2,S}\mathbf{I} \\ \vdots & \vdots & \ddots & \vdots \\ z_{hw,1}\mathbf{I} & z_{hw,2}\mathbf{I} & \cdots & z_{hw,S}\mathbf{I} \end{bmatrix}$  and  $\text{vec}(\mathbf{A}) = [a_{11}, \dots, a_{S1}, a_{12}, \dots, a_{S2}, \dots, a_{1s}, \dots, a_{Ss}]^T$ .

$\mathbf{BY} = \mathbf{ZA}$  has a nonzero solution for  $\mathbf{B}$  and  $\mathbf{A}$

$$\Leftrightarrow \begin{aligned} & \bullet (HW \geq s) \text{ or } (HW < s \text{ and } hw < \frac{Ss}{s-HW}) \\ & \bullet (HW < s \text{ and } hw \geq \frac{Ss}{s-HW}) \text{ and } \text{rank}([\mathbf{Z}_{hw \times S} \otimes \mathbf{I}_{s \times s}, -\mathbf{I}_{hw \times hw} \otimes \mathbf{Y}_{s \times HW}^T]) < \min(hws, Ss + hwHW). \end{aligned}$$

The subscripts on the matrices are just to emphasize the shape of each matrix. The theorem demonstrates that if the high-resolution space  $HW$  is bigger than the low spectral number  $s$ , then there exists a non-zero solution for  $\mathbf{A}$  and  $\mathbf{B}$ .

**Down-sampling enhancement:** By constructing down-sampling matrix  $\hat{\mathbf{B}}$  to obtain  $\mathbf{B} = \mathbf{Z}\mathbf{Z}^+\hat{\mathbf{B}}$ , it yields  $\mathbf{BY} = \mathbf{Z}(\mathbf{Z}^+\hat{\mathbf{B}}\mathbf{Y}) = \mathbf{ZA}$ . As a result, the solution turns out to be

$$\mathbf{A} = \mathbf{Z}^+\hat{\mathbf{B}}\mathbf{Y}, \quad (7)$$

where  $\mathbf{Z}^+$  is the Moore-Penrose generalized inverse of  $\mathbf{Z}$ . If we assume  $\text{rank}(\mathbf{Z}) = S$  it can be further represented as  $\mathbf{Z}^+ = (\mathbf{Z}^T\mathbf{Z})^{-1}\mathbf{Z}^T$ . The above formula also provides a optimal solution under the least square criterion [37] for

$$\mathbf{A} = \arg \min_{\mathbf{M}} \|\hat{\mathbf{B}}\mathbf{Y} - \mathbf{Z}\mathbf{M}\|. \quad (8)$$

In the subsequent theoretical discussion of error analysis, the use of down-sampling enhancement will induce the equivalence of the CS method and the MRA method. Experiments demonstrate that this enhancement results in better quantitative and qualitative outcomes for both CS and MRA methods.

#### E. Solutions for $\mathbf{X}$

If we rewrite the form of **Assumption II.1** as linear equations with respect to  $\text{vec}(\mathbf{X})$ , it yields

$$\begin{bmatrix} \mathbf{A}^T \otimes \mathbf{I} \\ \mathbf{I} \otimes \mathbf{B} \end{bmatrix} \text{vec}(\mathbf{X}) = \begin{bmatrix} \text{vec}(\mathbf{Y}) \\ \text{vec}(\mathbf{Z}) \end{bmatrix}. \quad (9)$$

As we can see from the Kronecker form, the problem we want to solve is a system of linear equations. The following theorem will provide one kind of solution to the system of linear equations.

**Theorem II.5.** [36], if the matrix equations in **Assumption II.1** have a solution, then one solution format to the **Assumption II.1** is the following:

$$\mathbf{X}_{mra} = \mathbf{B}^- \mathbf{Z} + (\mathbf{I} - \mathbf{B}^- \mathbf{B}) \mathbf{Y} \mathbf{A}^-, \quad (10)$$

According to [35], the general solution space is

$$\mathbf{X} = \mathbf{X}_{mra} + (\mathbf{I} - \mathbf{B}^- \mathbf{B}) \mathbf{W} (\mathbf{I} - \mathbf{A} \mathbf{A}^-), \quad (11)$$

where  $\mathbf{W} \in R^{HW \times S}$  is an arbitrary matrix.

$= 0$ , This corresponds to the MRA method. The first term  $\mathbf{B}^- \mathbf{Z}$  corresponds to the up-sampling MS images. The second term  $(\mathbf{I} - \mathbf{B}^- \mathbf{B}) \mathbf{Y} \mathbf{A}^-$  corresponds to the spectral up-sampling of the difference between the PAN image and the low-pass PAN image. Different selections of  $B^-$  and  $A^-$  yield different MRA methods. Since we have derived the general solution space, we can use prior knowledge to further optimize  $\mathbf{W}$ , thereby refining the MRA methods.

Inspire by this solution, we derive another general solution, which is

$$\mathbf{X} = \mathbf{B}^- \mathbf{Z} + (\mathbf{Y} - \mathbf{B}^- \mathbf{Z} \mathbf{A}) \mathbf{A}^-. \quad (12)$$

**Theorem II.6.** If the matrix equations in **Assumption II.1** have a solution, then one solution format of the **Assumption II.1** is the following

$$\mathbf{X}_{cs} = \mathbf{B}^- \mathbf{Z} + (\mathbf{Y} - \mathbf{B}^- \mathbf{Z} \mathbf{A}) \mathbf{A}^-, \quad (13)$$

and the general solution space is

$$\mathbf{X} = \mathbf{X}_{cs} + (\mathbf{I} - \mathbf{B}^- \mathbf{B}) \mathbf{W} (\mathbf{I} - \mathbf{A} \mathbf{A}^-), \quad (14)$$

where  $\mathbf{W} \in R^{HW \times S}$  is an arbitrary matrix.

This solution leads to the CS method. The first term  $\mathbf{B}^- \mathbf{Z}$  corresponds to the up-sampling MS images. The second term  $(\mathbf{Y} - \mathbf{B}^- \mathbf{Z} \mathbf{A}) \mathbf{A}^-$  corresponds to the spectral up-sampling of the difference between the PAN image and the synthetic PAN image. Different selections of  $B^-$  and  $A^-$  yield different CS methods. Since we have derived the general solution space for CS methods, we can use prior knowledge to further optimize  $\mathbf{W}$ , thereby refining the CS methods. The following theorem shows the relationship between two different representations.

**Theorem II.7.** If the matrix equation in **Assumption II.1** has a solution, then for fixed  $\mathbf{A}^- \in \mathbf{A}\{-\}$  and  $\mathbf{B}^- \in \mathbf{B}\{-\}$ ,  $\mathbf{X}_{cs} = \mathbf{X}_{mra}$ .

We will show that the traditional state-of-the-art method, GSA methods, can follow our CS generalized inverse solution representation.

#### F. Gram-Schmidt adaptive method

**Theorem II.8.** The Gram-Schmidt adaptive method can be described as follows. Suppose  $\text{var}(\mathbf{ZA})$  is invertible. Define

$$\mathbf{W} = \text{var}(\mathbf{ZA})^{-1} \text{cov}(\mathbf{ZA}, \mathbf{Z}) \in \mathbf{A}\{-\} \quad (15)$$

where

$$\text{cov}(\mathbf{ZA}, \mathbf{Z}) = \frac{1}{hw} (\mathbf{ZA} - \mathbf{1} \frac{\mathbf{1}^T}{hw} \mathbf{ZA})^T (\mathbf{Z} - \mathbf{1} \frac{\mathbf{1}^T}{hw} \mathbf{Z}),$$

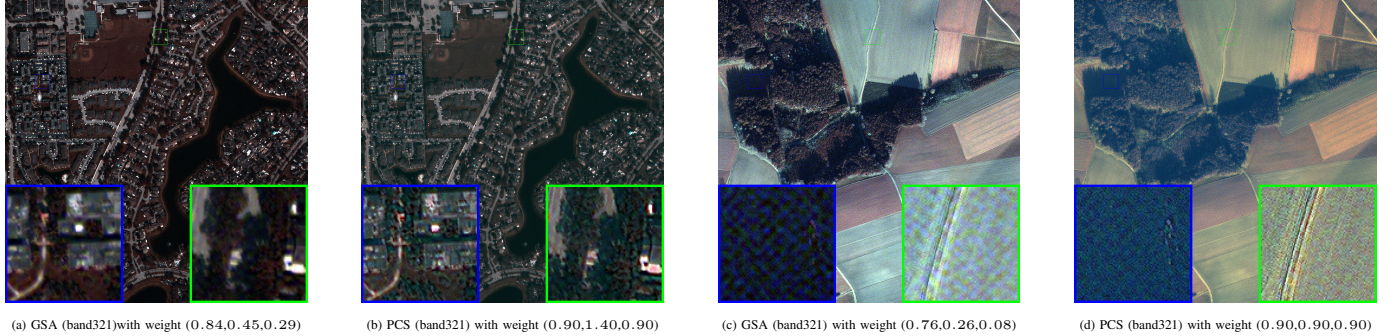


Fig. 1: Visual comparisons of the synthetic results with different values of elements in  $\mathbf{A}^-$ . The first two images come from W2 Miami Mix dataset and second two images come from W3 Muni Nat dataset. We select the 1,2,3 band from the eight bands of the data to illustrate the difference. The differences between the images arise solely from the values of elements in  $\mathbf{A}^-$ . When the elements are close to 0, then the image becomes blurred. Conversely, when the elements are close to 1, then the image becomes sharp.

$$\text{var}(\mathbf{ZA}) = \frac{1}{hw}(\mathbf{ZA} - \mathbf{1}\frac{\mathbf{1}^T}{hw}\mathbf{ZA})^T(\mathbf{ZA} - \mathbf{1}\frac{\mathbf{1}^T}{hw}\mathbf{ZA}), \quad (16)$$

It yields

$$\mathbf{X}_{g\mathbf{s}\mathbf{a}} = \mathbf{B}^-\mathbf{Z} + (\mathbf{Y} - \mathbf{B}^-\mathbf{ZA})\mathbf{W}. \quad (17)$$

The Gram-Schmidt adaptive method can be viewed as a special case of the representation in Theorem II.6. It yields

$$\mathbf{Y} = \mathbf{X}_{g\mathbf{s}\mathbf{a}}\mathbf{A} \quad (18)$$

$$\mathbf{Z} = \mathbf{B}\mathbf{X}_{g\mathbf{s}\mathbf{a}}. \quad (19)$$

Since GSA is a special case of the CS method, it shares the same representation of the general solution space. This allows it to be further refined and optimized using potential prior knowledge, such as a diffusion prior.

#### G. Model prior

An improper  $\mathbf{A}^-$  will lead to unrealistic results for  $\mathbf{X}$ , especially causing blurred features. Empirically, we found that when the elements of  $\mathbf{A}^-$  are much smaller than 1, it leads to a blurred image and when the elements of  $\mathbf{A}^-$  are close to 1, it lead to a sharp image. The visual comparison of the differences induced by the elements values can be seen in the Figure 1. We can embed the prior knowledge of the high spatial and spectral resolution by empirically assuming the search space of  $\mathbf{A}^-$  to be the *Uniform*( $[0.9, 1.4]^{1 \times S} \cap \{\mathbf{A}^- | \mathbf{A}\mathbf{A}^- \mathbf{A} = \mathbf{A}\}$ )<sup>1</sup> distribution among different sensors.

If  $s = 1$ , alternatively, it turns to be

$$\mathbf{A}^- = \{\mathbf{M} \in [0.9, 1.4]^{1 \times S} | \mathbf{A}\mathbf{M}\mathbf{A} = \mathbf{A}\}. \quad (20)$$

1) *Algorithm*: The algorithms are presented in Algorithms 1 and 2. We calculate the computational complexity of our methods and the GSA method. The complexity for our two methods is  $O(hwS \min(hw, S) + HWS + S^2)$ . The complexity for the GSA method is  $O(HWS + hwS \min(hw, S))$ . The  $S^2$  term can be omitted if  $S$  is smaller than  $HW$ .

<sup>1</sup>The paper's experiments mainly discuss the  $s = 1$  case

---

#### Algorithm 1 Prior Component substitution(CS) method

---

**Input:**  $(\mathbf{Y}, \mathbf{Z}, \mathbf{B}, \mathbf{B}^-)$ : The HrLS image, LrHS image, spatial response function matrix and up-sampling matrix;

**Output:**  $\mathbf{X}$

- 1: Construct the spatial up-sampling matrix  $\mathbf{B}^-$  and spatial down-sampling response matrix  $\hat{\mathbf{B}}$  closely approximating the sensor response function, satisfying  $\hat{\mathbf{B}}\mathbf{B}^- = \mathbf{I}$ .
  - 2: Obtain  $\mathbf{A} = \mathbf{Z}^+\hat{\mathbf{B}}\mathbf{Y}$  where  $\mathbf{Z}^+ = (\mathbf{Z}^T\mathbf{Z})^{-1}\mathbf{Z}^T$ .
  - 3: Obtain  $\mathbf{A}^- \in [0.9, 1.4]^{1 \times S}$  by solving  $\mathbf{A}\mathbf{A}^-\mathbf{A} = \mathbf{A}$ . It can be simplified to  $\mathbf{A}^-\mathbf{A} = 1$ .
  - 4: Synthesize low resolution low spectral LrLs  $\mathbf{ZA}$ .
  - 5: Upsample  $\mathbf{Z}$  and  $\mathbf{ZA}$  to obtain  $\mathbf{B}^-\mathbf{Z}$  and  $\mathbf{B}^-\mathbf{ZA}$ .
  - 6: Obtain  $\mathbf{X} = \mathbf{B}^-\mathbf{Z} + (\mathbf{Y} - \mathbf{B}^-\mathbf{ZA})\mathbf{A}^-$ .
- 

#### Algorithm 2 Prior Multiresolution analysis(MRA) method

---

**Input:**  $(\mathbf{Y}, \mathbf{Z}, \mathbf{B}, \mathbf{B}^-)$ : The HrLS image, LrHS image, spatial response function matrix and up-sampling matrix;

**Output:**  $\mathbf{X}$

- 1: Construct the spatial up-sampling matrix  $\mathbf{B}^-$  and spatial down-sampling response matrix  $\hat{\mathbf{B}}$  closely approximating to the sensor response function, satisfying  $\hat{\mathbf{B}}\mathbf{B}^- = \mathbf{I}$ .
  - 2: Obtain  $\mathbf{A} = \mathbf{Z}^+\hat{\mathbf{B}}\mathbf{Y}$  where  $\mathbf{Z}^+ = (\mathbf{Z}^T\mathbf{Z})^{-1}\mathbf{Z}^T$ .
  - 3: Obtain  $\mathbf{A}^- \in [0.9, 1.4]^{1 \times S}$  by solving  $\mathbf{A}\mathbf{A}^-\mathbf{A} = \mathbf{A}$ . It can be simplified to  $\mathbf{A}^-\mathbf{A} = 1$ .
  - 4: Synthesize low resolution low spectral(LrLs) image  $\mathbf{BY}$ .
  - 5: Upsample  $\mathbf{Z}$  and  $\mathbf{BY}$  to obtain  $\mathbf{B}^-\mathbf{Z}$  and  $\mathbf{B}^-\mathbf{BY}$ .
  - 6: Obtain  $\mathbf{X} = \mathbf{B}^-\mathbf{Z} + (\mathbf{Y} - \mathbf{B}^-\mathbf{BY})\mathbf{A}^-$ .
- 

#### H. Error analysis

If we take the up-sampling operator  $\mathbf{V}$  as  $\mathbf{B}^-$ , empirically  $\mathbf{B}\mathbf{B}^- = \mathbf{I}$ , but  $\mathbf{BV} = \mathbf{I}$  may not always hold. However, different algorithms may choose different  $\mathbf{A}^-$ . Negotiation with prior knowledge may lead to  $\mathbf{A}^-$  not being in  $\mathbf{A}\{-\}$ . We denote  $\mathbf{A}^-$  in this case as  $\mathbf{W}$ . Further error analysis can be conducted.

1) *Component substitution form analysis*:

**Theorem II.9.** If  $\mathbf{X}_{\text{recover}} = \mathbf{V}\mathbf{Z} + (\mathbf{Y} - \mathbf{V}\mathbf{ZA})\mathbf{W}$ , then

$$\mathbf{X}_{recover} \mathbf{A} - \mathbf{Y} = (\mathbf{VZ} \mathbf{A} - \mathbf{Y})(\mathbf{I} - \mathbf{WA}).$$

**Theorem II.10.** If  $\mathbf{X}_{recover} = \mathbf{VZ} + (\mathbf{Y} - \mathbf{VZ} \mathbf{A})\mathbf{W}$ , then  $\mathbf{B} \mathbf{X}_{recover} - \mathbf{Z} = (\mathbf{BV} - \mathbf{I})\mathbf{Z} + (\mathbf{BY} - \mathbf{BVZ} \mathbf{A})\mathbf{W}$ .

These two theorems demonstrate the spatial error and spectral error induced by up-sampling operator and  $\mathbf{A}^-$ .

2) *Multiresolution analysis form analysis:*

**Theorem II.11.** If  $\mathbf{X}_{recover} = \mathbf{VZ} + (\mathbf{Y} - \mathbf{VBY})\mathbf{W}$ , then  $\mathbf{X}_{recover} \mathbf{A} - \mathbf{Y} = \mathbf{V}(\mathbf{ZA} - \mathbf{BY}) - (\mathbf{I} - \mathbf{VB})\mathbf{Y}(\mathbf{I} - \mathbf{WA})$ .

**Theorem II.12.** If  $\mathbf{X}_{recover} = \mathbf{VZ} + (\mathbf{Y} - \mathbf{VBY})\mathbf{W}$ , then  $\mathbf{B} \mathbf{X}_{recover} - \mathbf{Z} = (\mathbf{BV} - \mathbf{I})\mathbf{Z} + (\mathbf{B} - \mathbf{BVB})\mathbf{YW}$ .

These two theorems demonstrate the spatial error and spectral error induced by up-sampling operator and  $\mathbf{A}^-$ .

**Theorem II.13.** With down-sampling enhancement(DSE), the prior component substitution method and prior multiresolution analysis methods are equivalent. That is If  $\mathbf{B} = \mathbf{ZZ}^+ \hat{\mathbf{B}}$  and  $\mathbf{A} = \mathbf{Z}^+ \hat{\mathbf{B}} \mathbf{Y}$ , then  $\mathbf{X}_{mra} = \mathbf{VZ} + (\mathbf{I} - \mathbf{VB})\mathbf{YA}^- = \mathbf{X}_{cs} = \mathbf{VZ} + (\mathbf{Y} - \mathbf{VZA})\mathbf{W}$ .

This theorem demonstrates that with down-sampling enhancement, the effect of our proposed methods can be the same.

3) *Total Analysis:*

**Theorem II.14.** If the Assumption II.1 has a solution, then the ground truth  $\mathbf{X}$  and  $\mathbf{X}_{mra}$  is different as follows,

$$\mathbf{X} - \mathbf{X}_{mra} = (\mathbf{I} - \mathbf{B}^- \mathbf{B})\mathbf{X}(\mathbf{I} - \mathbf{AA}^-). \quad (21)$$

This theorem suggests that we could further determine  $(\mathbf{I} - \mathbf{B}^- \mathbf{B})\mathbf{X}(\mathbf{I} - \mathbf{AA}^-)$  to obtain a better solution.

### I. The diffusion prior for Pan-sharpening

We could further employ diffusion prior to help determine best performance  $\mathbf{X}$  as follows:

$$\max_{\mathbf{W}} p_{diffusion\ model}(\mathbf{X}_{recover} + (\mathbf{I} - \mathbf{B}^- \mathbf{B})\mathbf{W}(\mathbf{I} - \mathbf{AA}^-)), \quad (22)$$

where  $\mathbf{X}_{recover}$  can be  $\mathbf{X}_{cs}$ ,  $\mathbf{X}_{mra}$  or  $\mathbf{X}_{gsa}$ . Since  $p_{diffusion\ model}$  is intractable, we replace it with the evidence lower bound  $ELBO_{\theta}$  [38] to derive the following:

$$\begin{aligned} \max_{\mathbf{W}} \quad & ELBO_{\theta}(\mathbf{X}_{recover} + (\mathbf{I} - \mathbf{B}^- \mathbf{B})\mathbf{W}(\mathbf{I} - \mathbf{AA}^-)) \\ = \quad & - \sum_{t=1}^T \mathbb{E}_{\varepsilon_0} \left\| \hat{\varepsilon}_{\theta}(\sqrt{\bar{\alpha}_t}(\mathbf{X}_{recover} + (\mathbf{I} - \mathbf{B}^- \mathbf{B})\mathbf{W}(\mathbf{I} - \mathbf{AA}^-) + \sqrt{1 - \bar{\alpha}_t} \varepsilon_0, t) - \varepsilon_0) \right\|^2 \end{aligned}$$

where  $\bar{\alpha}_t$  are the schedule parameters in the diffusion model [38],  $\hat{\varepsilon}_{\theta}$  is the U-Net function in the diffusion model [38], samples noises  $\varepsilon_0 \sim \mathcal{N}(0, \mathbf{I})$ ,  $T$  is total time of the time scheduler of the diffusion model [38].

By sample  $t$  [38], it yields

$$\begin{aligned} \min_{\mathbf{W}} \quad & \mathbb{E}_{\varepsilon_0, t} \left\| \hat{\varepsilon}_{\theta}(\sqrt{\bar{\alpha}_t}(\mathbf{X}_{recover} + (\mathbf{I} - \mathbf{B}^- \mathbf{B})\mathbf{W}(\mathbf{I} - \mathbf{AA}^-) + \sqrt{1 - \bar{\alpha}_t} \varepsilon_0, t) - \varepsilon_0) \right\|^2. \end{aligned}$$

One could use gradient descent on Equation 23 to optimize  $\mathbf{W}$ , thereby obtaining a refined result with diffusion prior by

---

**Algorithm 3** Pan-sharpening via Generalized-Inverse-Guided Diffusion Models

**Input:**  $(\mathbf{X}_{recover}, \mathbf{A}, \mathbf{B}, \mathbf{A}^-, \mathbf{B}^-, \hat{\varepsilon}_{\theta}, \bar{\alpha}, m)$  Pan-sharpened image, spectral down-sampling matrix, spatial down-sampling matrix, spectral up-sampling matrix, spatial up-sampling matrix, diffusion model, schedule, iteration steps

**Output:**  $\mathbf{X}_{recover} + (\mathbf{I} - \mathbf{B}^- \mathbf{B})\mathbf{W}(\mathbf{I} - \mathbf{AA}^-)$

Initialize  $\mathbf{W}$  as  $\mathbf{0}$

**for**  $i = 1$  **to**  $m$  **do**

Randomly initialize  $\varepsilon_0 \sim \mathcal{N}(0, \mathbf{I})$ ,  $t \sim Uniform(1, \dots, T)$ .

Take gradient step on

$\nabla_{\mathbf{W}} \text{dot}(\text{stopgradient}[\hat{\varepsilon}_{\theta}(\sqrt{\bar{\alpha}_t}(\mathbf{X}_{recover} + (\mathbf{I} - \mathbf{B}^- \mathbf{B})\mathbf{W}(\mathbf{I} - \mathbf{AA}^-) + \sqrt{1 - \bar{\alpha}_t} \varepsilon_0, t) - \varepsilon_0), (\mathbf{X}_{recover} + (\mathbf{I} - \mathbf{B}^- \mathbf{B})\mathbf{W}(\mathbf{I} - \mathbf{AA}^-))])$

**end for**

---

searching in the general solution space. We use Score Distillation Sampling [39] to accelerate optimization. Algorithm 3 describes the each step of our model. It demonstrates that once we have a foundational diffusion model and identify the general solution spaces for CS and MRA methods with the help of generalized inverse theory, we can search within these solution spaces to refine Pan-sharpening techniques (for example, the GSA method).

## III. EXPERIMENTS AND RESULTS

We will first introduce the evaluation measures, and then the datasets that we use to compare our methods and finally provide the experiments on these datasets.

### A. Evaluation measures.

Five quantitative evaluation indices are employed for performance evaluation, including consistent root mean square error(Consistent RMSE), spatial root mean square error(Spatial RMSE), spectral root mean square error(Spectral RMSE), Inverse Ability, and root mean square error(RMSE).

**Definition III.1.** Consistent root mean square error(Consistent RMSE) refers to

$$\sqrt{\frac{1}{hws} \|\mathbf{ZA} - \mathbf{BY}\|_F^2}. \quad (24)$$

The Consistent RMSE reflects the consistency of the spatial and spectral response function. Consistent RMSE= 0 is a necessary condition for the problem to have a solution.

**Definition III.2.** Spatial root mean square error(Spatial RMSE) refers to

$$\sqrt{\frac{1}{Hws} \|\mathbf{X}_{recover} \mathbf{A} - \mathbf{Y}\|_F^2}. \quad (25)$$

The mean spatial root mean square error refers to the mean Spatial RMSE of the whole dataset.

Spatial RMSE measures the spatial consistency between the recovered HrHS image and the HrLS image.

**Definition III.3.** Spectral root mean square error(Spectral RMSE) refers to

$$\sqrt{\frac{1}{hws} \|\mathbf{B}\mathbf{X}_{recovered} - \mathbf{Z}\|_F^2}. \quad (26)$$

The mean spectral root mean square error refers to the mean Spectral RMSE of the entire dataset.

Spectral RMSE measures the spectral consistency between the recovered HrHS image and the HrLS image.

**Definition III.4.** Inverse Ability refers to  $\mathbf{A}^{-1}\mathbf{A}$ .

The inverse ability of the  $\mathbf{A}^{-1}$  is an important index influencing both Spectral RMSE and Spatial RMSE. The closer  $\mathbf{A}^{-1}\mathbf{A}$  is to 1, the better.

**Definition III.5.** Root mean square error(RMSE) refers to

$$\sqrt{\frac{1}{hws} \|\mathbf{X} - \mathbf{X}_{recover}\|_F^2}. \quad (27)$$

Root mean square error reflects the distance between the recovered image and the oracle image.

We also implemented SAM,EGRAS [40] for our synthetic experiments. However, we found they can not effectively reflect the advantage related to visual appearance(sharper results) of our method. As a result, we didn't show them in our experiment tables.

For the diffusion-related experiment, since ground truth data is available, we use RMSE, spatial RMSE, spectral RMSE, PSNR [41], SSIM [41], SAM, and ERGAS to evaluate our model's performance and fully demonstrate its advantages.

### B. Dataset description.

#### Dataset description for the WV3 New York dataset [42].

The WorldView-3 ground sample distance is 0.31m for the PAN band and 1.24m for eight MS bands. WV3 imagery of New York City (USA) reveals a cityscape characterized by tall buildings. (The size of an MS spectral band is 512×512). Since many other algorithms have been compared on this dataset, we use this dataset to compare the spatial RMSE and spectral RMSE of our methods and the other methods, including CS methods, MRA methods, VO methods and Deep learning methods.

**Dataset description for the Chikusei dataset.** The Chikusei dataset [43] consists of 2517×2335 pixels. The grid length is 2.5m. The central point is located at coordinates: 36.294946 degrees north, 140.008380 degrees east. The data was acquired at urban areas in Chikusei, Ibaraki, Japan on July 29, 2014. It has 128 bands. This dataset aims to verify the Pan-sharpening ability on HS data.

**Dataset description for the PAirMax dataset.** The PAirMax dataset [40] is composed of 14 PAN and MS image pairs which are collected over different landscapes by various satellites. The detailed parameters for different satellite images are as follows:

- The GeoEye-1 ground sample distance is 0.46m for the PAN band and 1.84m for the blue, green, red and near infrared bands.

- The WorldView-2 ground sample distance is 0.46m for the PAN band and 1.84m for eight MS bands.
- The WorldView-3 ground sample distance is 0.31m for the PAN band and 1.24m for eight MS bands.
- The WorldView-4 ground sample distance is 0.31m for the PAN band and 1.24m for the four MS bands.
- The SPOT-7 ground sample distance is 1.5m for the PAN band and 6m for the four MS bands.
- Pléiades-1B ground sample distance is 0.7m for the PAN band and 2.8m for the four MS bands.

The experiments on this dataset focus on ablation study.

**Dataset description for the PAirMax-RGB dataset.** To validate the performance of the diffusion model (trained on Imagenet [44], named “256x256\_diffusion\_uncond.pt”), we created an RGB image sub-dataset derived from PAirMax. The RGB channels of ground truth image correspond to the RGB channels of the original MS\_LR image from the FF path. We cropped the upper-left 256 × 256 pixels region of the MS\_LR images and applied percentile stretching (0.25%-99.75%) to process the images, resulting in the final RGB ground truth images. For experiment simplification, the PAN image was generated by averaging the RGB image channels with equal weighting. This dataset contains a total of 9 ground truth images and is referred to as PAirMax-RGB.

### C. Comparison methods

We evaluate the different methods in comparison with state-of-art methods. For WV3 New York dataset, the comparison methods include our methods(PCS and PMRA) and methods in the literature [42] [45]. Since we used the same dataset, same comparison methods and their codes [42] [45], the visual appearances of different comparison methods are consistent with the results in [42].

For Chikusei dataset and PAirMax dataset, we focus on the comparison of our methods with those methods that align with the generalized inverse illustration. The comparison methods include: GSA [46], MTF-GLP-CBD [47], Prior component substitution(PCS), Prior multiresolution analysis (PMRA).For PAirMax dataset, we also compare the methods with(without) the down-sampling enhancement(DSE).

For PAirMax-RGB, we focus on the validating the improvement of our methods combining with the diffusion priors. The comparison methods include: GSA, GSA+diffusion, MTF-GLP-CBD, PCS, and PCS +diffusion.

### D. Experimental model training settings

For the diffusion model used in Pan-sharpening, we implemented the experiment using PyTorch. The training was conducted on an NVIDIA GeForce RTX 3060(12G). The diffusion process employs a linear schedule with 1,000 timesteps. We utilize the Adam optimizer [48] with a learning rate of  $10^{-2}$  for gradient-based optimization of the parameter matrix  $\mathbf{W}$ . Approximately 2000 iterations are required to optimize  $\mathbf{W}$ , and the process takes roughly 10 minutes to produce a single image.

TABLE I: Full-resolution comparison experiments on WV3 New York Dataset

Method	Spectral RMSE(↓)	Spatial RMSE(↓)
EXP [42]	<b>4.5452</b>	109.2157
BT-H [13]	71.6169	<b>17.8711</b>
BDSD-PC [15]	114.9423	74.8058
C-GSA [12]	75.4264	26.8394
SR-D [16]	100.4333	107.7014
MTF-GLP-HPM-R [5]	74.2957	63.7501
MTF-GLP-FS [7]	71.2183	58.1442
TV [17]	97.7862	61.4820
PanNet [49]	83.1296	71.4575
DRPN [25]	83.2450	42.0010
MSDCNN [26]	84.7197	45.3580
BDPN [28]	85.6572	39.7455
DiCNN [27]	88.2270	73.7617
PNN [19]	121.9181	69.4336
APNN [29]	79.4560	52.2568
FusionNet [30]	107.6745	122.9544
<b>PCS/PMRA</b>	10.0245	<b>5.4193</b>

#### E. Comparative experiments: performance comparison on WV3 New York

In the experiment, bilinear down-sampling was selected as the spatial down-sampling matrix for calculating the spectral RMSE. The spectral weighting matrix was computed using our proposed method. Here we mainly present the full-resolution experiments to highlight the good consistency of our method.

1) *Quantitative results*: According to table I, the quantitative result demonstrates that PCS/PMRA methods (with down-sampling enhancement) are relatively better than the other 16 methods except for the spectral RMSE of the EXP method. Since EXP method is the interpolation of MS image using a polynomial kernel, its spatial RMSE is notably high. In contrast, both the spatial RMSE and spectral RMSE values for the PCS/PMRA Methods (with down-sampling enhancement) are near zero.

2) *Qualitative results*: According to Figure 2, our methods, PCS and PMRA, are clear and the color is realistic, while there are strange textures on the results of PanNet, DRPN, MSDCNN, DiCNN, PNN, APNN, FusionNet.

#### F. Synthetic experiments: performance comparison with Chikusei data

1) *Generation of the simulated data*: We implemented two experiments. In the first experiment, we used equal weights for all bands to generate the PAN image and employed 2-scale mean down-sampling to generate the low spatial resolution HS image. Since the resolution of first experiment was high, we also used it for visual demonstration. In the second experiment, we uniformly sampled weights from 0.1 to 1 and linearly normalized the weights to sum to 1, and used these normalized weights to generate the PAN image. We then employed 4-scale mean down-sampling to generate the low spatial resolution HS image.

We consider the  $s = 1$  situation. We choose the number 60, 40, and 21 bands to represent the red, green, and blue (RGB) spectral channels for rendering real color images. Additionally, we select the number 50, 27, and 11 bands

to represent orange, azure, and purple (OAP) for rendering synthetic images.

TABLE II: Chikusei synthetic experiments

(a) Equally weighted PAN and 2-scale mean down-sampling HS					
Method	Consistent RMSE(↓)	Spatial RMSE(↓)	Spatial RMSE(↓)	RMSE(↓)	$\mathbf{A}^{\perp} \mathbf{A}$
MTF-GLP-CBD	0.00	0.00	47.12	79.25	1.00
GSA	0.00	0.00	47.12	79.25	1.00
PCS	0.00	0.00	55.70	93.93	1.00
PMRA	0.00	0.00	55.70	93.93	1.00

(b) Randomly weighted PAN and 4-scale mean down-sampling HS					
Method	Consistent RMSE(↓)	Spatial RMSE(↓)	Spatial RMSE(↓)	RMSE(↓)	$\mathbf{A}^{\perp} \mathbf{A}$
MTF-GLP-CBD	132.46	89.48	41.67	186.02	0.92
GSA	132.46	0.00	166.33	154.85	1.00
PCS	0.00	0.00	18.14	186.13	1.00
PMRA	0.00	0.00	18.14	186.13	1.00

2) *Existence of the solution*: According to table IIa, the *consistent RMSE* = 0 implies the solutions could exist. According to table IIb, the *consistent RMSE* for GSA and MTF-GLP-CBD are higher than that for PCS and PMRA since PCS and PMRA employ down-sampling enhancement techniques.

3) *Recover of the solution*: The recovered solutions for the first experiment are shown in Figure 3. According to Table IIa and Table IIb, all the methods in this experiment exhibit general invertibility for  $\mathbf{A}$  and  $\mathbf{A}^{\perp}$  except for MTF-GLP-CBD in the second experiment. Additionally, the spatial RMSE values for all four methods are zero except for the MTF-GLP-CBD in the second experiment. However, the spectral RMSE are non-zero, indicating that the down-sampling and up-sampling matrices are not matched. This mismatch arises because we employ bilinear interpolation for down-sampling and up-sampling operators to prioritize visual performance. The similar results of GSA and MTF-GLP-CBD in Table IIa may be due to the experiment setting (the construction of the PAN image).

Regarding RMSE, the proposed methods exhibit higher values compared to the GSA and MTF-GLP-CBD methods. This phenomenon may be due to a better match of  $\mathbf{A}^{\perp}$  and RMSE extracted by the GSA and MTF-GLP-CBD in these synthetic experiments. Since the prior for  $\mathbf{A}^{\perp}$  is designed to optimize visual quality, a minor deficiency in the proposed methods' RMSE is deemed acceptable.

The image results show that methods derived from the generalized inverse have good performance, while the proposed PCS and PMRA exhibit better visual sharpness.

#### G. Ablation study: performance comparison with PAirMax data

We used nine scenes in this dataset. The quantitative results reflect analyses from all nine scenes, while the qualitative results are based on experiments conducted using the GE Tren Urb dataset. We used the MS\_LR in the FF path to conduct the experiment. The mean down-sampling and nearest neighborhood up-sampling (which are matched) were selected for the algorithms and calculations of the spectral RMSE.

1) *Quantitative results*: DSE is used to denote down-sampling enhancement.

According to table IIIa, IIIb, IIIc, IIId, IIIe, IIIf, IIIg, IIIh, IIIi, the quantitative result shows that GSA and PCS/PMRA methods with down-sampling enhancement are relatively better than MTF-GLP-CBD and vanilla GSA, PCS, and PMRA



Fig. 2: Comparisons of the different Pan-sharpening methods [42] for WV3 New York dataset.

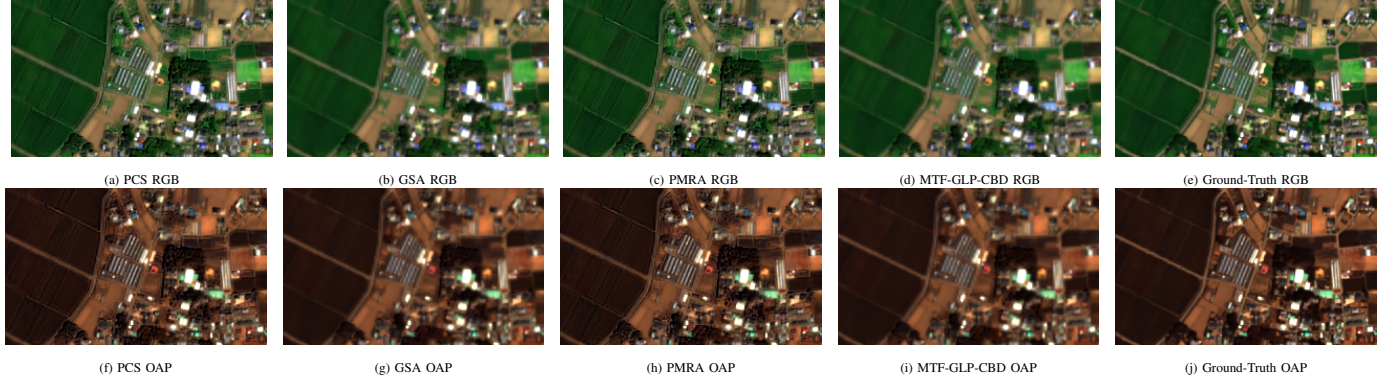


Fig. 3: Comparisons of the different synthetic methods with ground truth. RGB represents the red green blue channel and OAP represents the other selected three channels.

methods. The three losses(consistent RMSE, spatial RMSE, spectral RMSE) are all zero for the GSA and PCS/PMRA methods with down-sampling enhancement given  $\mathbf{A}^\top \mathbf{A} = 1$ .

TABLE III: Performance comparison on PAirMax data

(a) GE Lond Urb					
Method	DSE	Consistent RMSE(↓)	Spatial RMSE(↓)	Spectral RMSE(↓)	$\mathbf{A}^\top \mathbf{A}$
MTF-GLP-CBD	×	37.46	37.62	0.00	0.93
GSA	✓	3.74	1.00	0.00	1.00
PCS	×	37.36	0.00	36.13	1.00
PMRA	×	37.36	37.36	0.00	1.00
MTF-GLP-CBD	✓	0.00	5.17	0.00	0.93
GSA	✓	0.00	0.00	0.00	1.00
PCS/PMRA	✓	0.00	0.00	0.00	1.00
(b) GE Tree Urb					
Method	DSE	Consistent RMSE(↓)	Spatial RMSE(↓)	Spectral RMSE(↓)	$\mathbf{A}^\top \mathbf{A}$
MTF-GLP-CBD	×	41.83	41.96	0.00	1.00
GSA	✓	41.83	0.00	53.80	1.00
PCS	×	41.83	0.00	53.21	1.00
PMRA	×	41.83	41.83	0.00	1.00
MTF-GLP-CBD	✓	0.00	3.51	0.00	0.96
GSA	✓	0.00	0.00	0.00	1.00
PCS/PMRA	✓	0.00	0.00	0.00	1.00
(c) W2 Miami Mix					
Method	DSE	Consistent RMSE(↓)	Spatial RMSE(↓)	Spectral RMSE(↓)	$\mathbf{A}^\top \mathbf{A}$
MTF-GLP-CBD	×	26.94	27.04	0.00	0.96
GSA	✓	26.94	0.00	27.09	1.00
PCS	×	26.94	3.43	26.31	1.05
PMRA	×	26.94	27.12	0.00	1.05
MTF-GLP-CBD	✓	0.00	2.49	0.00	0.96
GSA	✓	0.00	0.00	0.00	1.00
PCS/PMRA	✓	0.00	0.00	0.00	1.00
(d) W2 Miami Urb					
Method	DSE	Consistent RMSE(↓)	Spatial RMSE(↓)	Spectral RMSE(↓)	$\mathbf{A}^\top \mathbf{A}$
MTF-GLP-CBD	×	46.77	46.85	0.00	0.97
GSA	✓	46.77	0.00	46.85	1.00
PCS	×	46.77	0.00	46.78	1.00
PMRA	×	46.77	46.77	0.00	1.00
MTF-GLP-CBD	✓	0.00	3.17	0.00	0.97
GSA	✓	0.00	0.00	0.00	1.00
PCS/PMRA	✓	0.00	3.45	0.00	1.05
(e) W3 Mun Mix					
Method	DSE	Consistent RMSE(↓)	Spatial RMSE(↓)	Spectral RMSE(↓)	$\mathbf{A}^\top \mathbf{A}$
MTF-GLP-CBD	×	13.58	13.64	0.00	0.96
GSA	✓	13.58	0.00	16.83	1.00
PCS	×	13.58	3.32	12.26	1.09
PMRA	×	13.58	13.93	0.00	1.09
MTF-GLP-CBD	✓	0.00	1.45	0.00	0.96
GSA	✓	0.00	0.00	0.00	1.00
PCS/PMRA	✓	0.00	3.33	0.00	1.09
(f) W3 Mun Nat					
Method	DSE	Consistent RMSE(↓)	Spatial RMSE(↓)	Spectral RMSE(↓)	$\mathbf{A}^\top \mathbf{A}$
MTF-GLP-CBD	×	5.44	5.45	0.00	0.98
GSA	✓	5.44	0.00	9.36	1.00
PCS	×	5.44	0.00	5.33	1.00
PMRA	×	5.44	5.44	0.00	1.00
MTF-GLP-CBD	✓	0.00	0.34	0.00	0.98
GSA	✓	0.00	0.00	0.00	1.00
PCS/PMRA	✓	0.00	0.00	0.00	1.00
(g) W3 Mun Urb					
Method	DSE	Consistent RMSE(↓)	Spatial RMSE(↓)	Spectral RMSE(↓)	$\mathbf{A}^\top \mathbf{A}$
MTF-GLP-CBD	×	26.40	26.59	0.00	0.94
GSA	✓	26.40	0.00	31.99	1.00
PCS	×	26.40	0.00	26.64	1.00
PMRA	×	26.40	26.40	0.00	1.00
MTF-GLP-CBD	✓	0.00	3.48	0.00	0.94
GSA	✓	0.00	0.00	0.00	1.00
PCS/PMRA	✓	0.00	0.00	0.00	1.00
(h) W4 Mexi Nat					
Method	DSE	Consistent RMSE(↓)	Spatial RMSE(↓)	Spectral RMSE(↓)	$\mathbf{A}^\top \mathbf{A}$
MTF-GLP-CBD	×	13.58	13.58	0.00	0.99
GSA	✓	13.58	0.00	14.40	1.00
PCS	×	13.58	0.00	12.70	1.00
PMRA	×	13.58	13.58	0.00	1.00
MTF-GLP-CBD	✓	0.00	0.21	0.00	0.99
GSA	✓	0.00	0.00	0.00	1.00
PCS/PMRA	✓	0.00	0.00	0.00	1.00
(i) W4 Mexi Urb					
Method	DSE	Consistent RMSE(↓)	Spatial RMSE(↓)	Spectral RMSE(↓)	$\mathbf{A}^\top \mathbf{A}$
MTF-GLP-CBD	×	40.80	40.86	0.00	0.97
GSA	✓	40.80	0.00	45.46	1.00
PCS	×	40.80	0.00	38.53	1.00
PMRA	×	40.80	40.80	0.00	1.00
MTF-GLP-CBD	✓	0.00	2.83	0.00	0.97
GSA	✓	0.00	0.00	0.00	1.00
PCS/PMRA	✓	0.00	0.00	0.00	1.00

2) *Qualitative results:* According to figure 4, we can see that GSA, GSA with DSE, PCS with DSE, PMRA with DSE, and MTF-GLP-CBD with DSE exhibit relatively better qualitative results. MTF-GLP-CBD and vanilla PMRA appear blurred and sawtooth-blocked. These results are consistent with the quantitative results presented in the tables. Additionally, it shows that down-sampling enhancement is not only beneficial for quantitative results but also effective for improving image appearance.

#### H. Diffusion-related experiments: performance comparison with PAirMax-RGB data

There are nine scenes in this dataset. The quantitative results reflect statistical analyses from all nine scenes, while the qualitative results are based on experiments conducted using the W4 Mexi Nat-RGB dataset.

1) *Quantitative results:* According to Table IV, The PCS+diffusion method achieves the best performance among all the evaluation measures. The GSA+diffusion method achieves the second-best performance. It demonstrates that employing a diffusion prior can significantly improve the Pan-sharpening results. Since we used average pooling and nearest up-sampling, the down-sampling and up-sampling matrix are matched and therefore spectral RMSE is zero. The similar results of GSA and MTF-GLP-CBD in this case may be due to the experiment setting (the construction of the PAN image).

TABLE IV: Comparison of different methods on PAirMax-RGB(mean  $\pm$  standard deviation). We left appropriate decimal places to facilitate the comparison of these methods.)

Method	RMSE (↓)	Spatial RMSE (↓)	Spectral RMSE(↓)	PSNR (↑)	SSIM (↑)	SAM (↓)	ERGAS (↓)
PCS	$0.0046 \pm 0.0023$	$0.00 \pm 0.00$	$0.00 \pm 0.00$	$47.58 \pm 3.89$	$0.9981 \pm 0.0012$	$1.15 \pm 0.37$	$9.62 \pm 2.78$
PCS+diffusion	<b><math>0.0030 \pm 0.0015</math></b>	$0.00 \pm 0.00$	$0.00 \pm 0.00$	<b><math>51.26 \pm 3.43</math></b>	<b><math>0.9990 \pm 0.0007</math></b>	<b><math>0.81 \pm 0.13</math></b>	<b><math>6.32 \pm 2.05</math></b>
GSA	$0.0068 \pm 0.0031$	$0.00 \pm 0.00$	$0.00 \pm 0.00$	$46.18 \pm 4.20$	$0.9974 \pm 0.0023$	$1.41 \pm 0.42$	$11.28 \pm 3.26$
GSA+diffusion	$0.0049 \pm 0.0021$	$0.00 \pm 0.00$	$0.00 \pm 0.00$	$49.01 \pm 3.97$	$0.9984 \pm 0.0012$	<b><math>1.14 \pm 0.30</math></b>	$8.14 \pm 2.27$
MTF-GLP-CBD	$0.0056 \pm 0.0031$	$0.00 \pm 0.00$	$0.00 \pm 0.00$	$46.18 \pm 4.20$	$0.9974 \pm 0.0023$	$1.44 \pm 0.42$	$11.28 \pm 3.26$

2) *Qualitative results:* According to Figure 5, all the methods demonstrate similar visual performances.

#### IV. LIMITATIONS AND DISCUSSIONS

Although our method demonstrates good results, our consideration of the generalized inverse in the Pan-sharpening

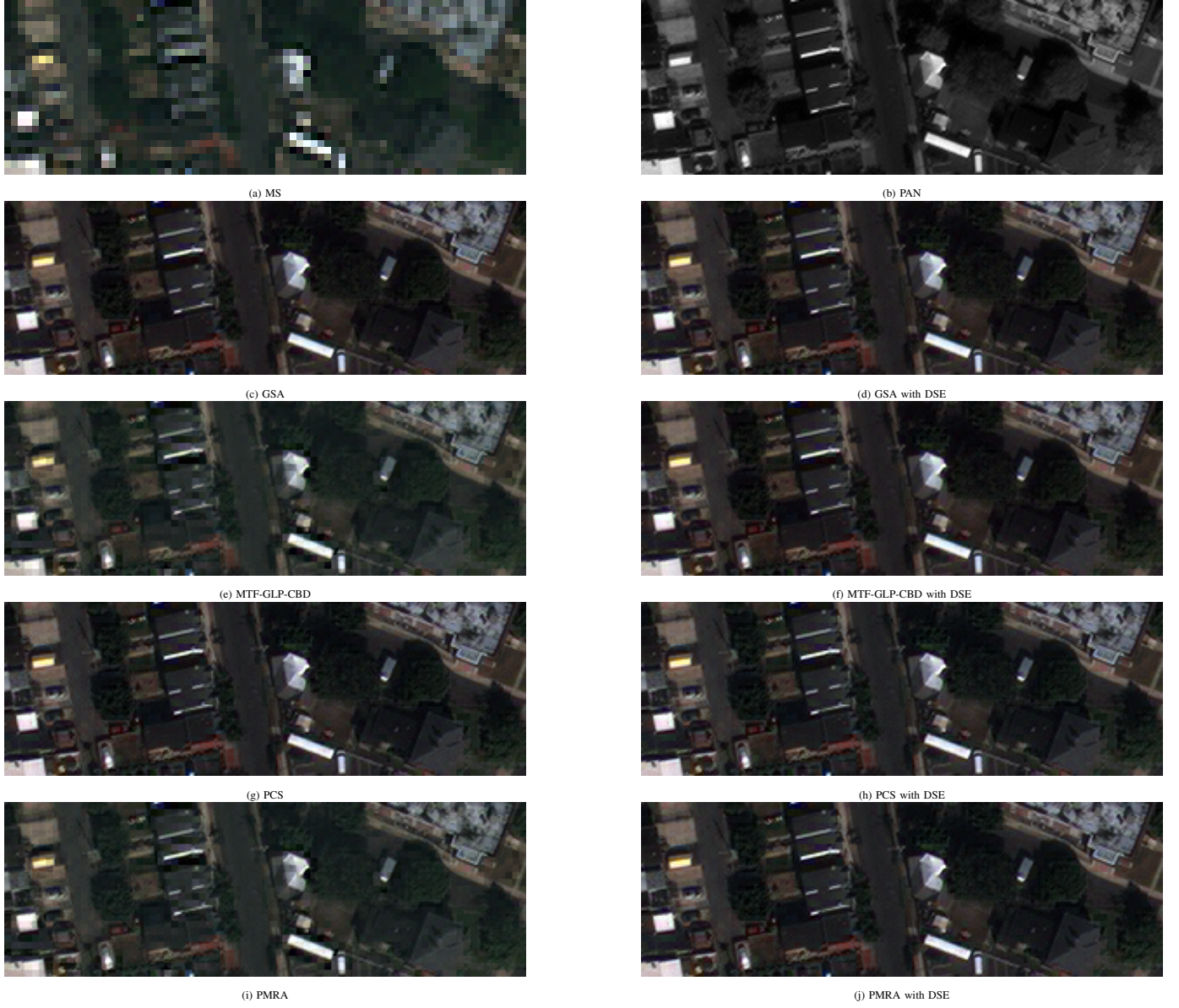


Fig. 4: Comparisons of the different methods for GE Tren Urb dataset.

problem limits  $s = 1$  in the prior setting section. We will explore the prior when  $s > 1$  in future work. Additionally, the spatial response functions and their inverse functions, including down-sampling and up-sampling matrices, utilize bilinear, mean or nearest neighbor functions for approximation. The spatial response functions may need to be accurately estimated, and their generalized inverse may need to be determined precisely. A current limitation is that the current spatial down-sampling matrix is assumed to be fully known. However, the specified spatial down-sampling process and the actual spatial down-sampling process may differ, which would further affect the calculation of the spectral down-sampling matrix to some extent. Since we have deduced the general solution space, in future work, we could let the model learn a proper spatial down-sampling matrix by searching within the prior knowledge provided by a diffusion model. Once this spatial down-sampling matrix is learned, we could derive a more

accurate spectral down-sampling matrix. As for the model prior, the relationship to the range of  $\mathbf{A}^-$  requires more dedicated exploration, and the spectral information of object information can be utilized by deep learning models.

Although our methods incorporate diffusion priors, the diffusion model currently used is based on ImageNet [50], which has only three spectral channels. This limits the applicability of our method. We believe that foundation diffusion models for remote sensing images—which do not yet exist—would be an effective way to extend the utility of our approach.

Although our mathematical models for CS and MRA are elegant, we have not yet considered the impact of noise on the model solution space. Since our method aligns with some existing CS and MRA frameworks, studying the effects of noise could naturally extend these methods into more robust forms. Further research into the influence of noise on our models remains an important area for future investigation.



Fig. 5: Comparisons of the different methods for W4 Mexi Nat-RGB dataset.

## V. CONCLUSION

In this paper, we utilize generalized inverse theory to understand and solve the matrix representation of the Pan-sharpening problem. By considering the generalized inverse of the matrices, we deduce a representation for the spectral response matrix with the help of the Moore–Penrose inverse. Specifically, we introduce down-sampling enhancement with Moore–Penrose inverse reprojection on the down-sampling matrix.

According to the [36], we find a high-spatial and high-spectral image solution space corresponding to the commonly used MRA Pan-sharpening regime using the generalized inverse. Similarly, we derive another high-spatial and high-spectral image solution space corresponding to the commonly used CS Pan-sharpening regime with the help of via the generalized inverse. Specifically, we prove that the GSA method is a special case of our generalized-inverse-based CS framework.

Based on the deduction of the CS and MRA, we propose a prior on the generalized inverse of the spectral response matrix. This yields algorithms for PCS and PMRA.

Since people may not use the exact generalized inverse to substitute in the PCS and PMRA regime, we analyze their error. Specifically, we deduce that under down-sample enhancement, PCS and PMRA are equivalent. Besides, we discuss the generalized inverse representation may differ from the oracle solution. The difference depends on the oracle solution, the generalized inverse of the down-sampling matrix, and the generalized inverse of the spectral response matrix.

To further incorporate the prior knowledge of the diffusion model, we substitute the general solution spaces of the generalized inverse form into the evidence lower bound of the diffusion model and optimize the auxiliary matrix  $\mathbf{W}$  by Score Distillation Sampling to obtain a refined Pan-sharpening solution.

According to the matrix representation of the Pan-sharpening problem, we use consistent RMSE, Spatial RMSE, Spectral RMSE, Inverse Ability, and RMSE to evaluate the models derived from the generalized inverse theories. In extensive comparison experiments, PCS and PMRA have lowest spatial and spectral RMSE, and their results are clear and sharp. In the synthetic experiments, PCS and PMRA's results are more clear and possess sharp boundaries. In the real data experiment for ablation study, we show that GSA, PCS, and PMRA with down-sample enhancement are quantitatively better, besides results of MTF-GLP-CBD and PMRA with down-sample enhancement are clear and possess sharp boundaries.

The effect of the proposed down-sample enhancement is also validated in both the qualitative and quantitative experiment results. The experiment conducted to validate the effect of the diffusion prior demonstrates that the diffusion prior can significantly improve the performance of PCS and GSA across almost all evaluation measures even though the generated images are visually similar. It demonstrates that after identifying the general solution spaces for CS and MRA methods via generalized inverse theory, we can search within these solution spaces to refine Pan-sharpening techniques.

## VI. DATA AVAILABILITY STATEMENTS

The hyperspectral data that support the findings of this study are openly available in <https://www.salt.u-tokyo.ac.jp/hyperdata/>. The PAirMax dataset data that support the findings of this study are openly available in <https://resources.maxar.com/product-samples/pansharpening-benchmark-dataset>. The WV3 New York dataset can be found in <https://github.com/liangjiandeng/DLPan-Toolbox> [42].

The authors confirm that the other data supporting the findings of this study are available within the article.

## ACKNOWLEDGEMENTS

We thank Xinlin Xie, Cong Liu, and Xuchen Zhang for the discussions on GSA methods. We also thank Fan Wang for sharing practical experience with regularized Bayesian GSA. We thank Xinyang Han for the discussion regarding the projection model.

## REFERENCES

- [1] Y. Zhang and R. K. Mishra, “A review and comparison of commercially available pan-sharpening techniques for high resolution satellite image fusion,” in *2012 IEEE International geoscience and remote sensing symposium*. IEEE, 2012, pp. 182–185.
- [2] G. Vivone, L. Alparone, J. Chanussot, M. Dalla Mura, A. Garzelli, G. A. Licciardi, R. Restaino, and L. Wald, “A critical comparison among pansharpening algorithms,” *IEEE Transactions on Geoscience and Remote Sensing*, vol. 53, no. 5, pp. 2565–2586, 2014.
- [3] P. Chavez, S. C. Sides, J. A. Anderson *et al.*, “Comparison of three different methods to merge multiresolution and multispectral data—landsat tm and spot panchromatic,” *Photogrammetric Engineering and remote sensing*, vol. 57, no. 3, pp. 295–303, 1991.
- [4] G. Vivone, R. Restaino, M. Dalla Mura, G. Licciardi, and J. Chanussot, “Contrast and error-based fusion schemes for multispectral image pansharpening,” *IEEE Geoscience and Remote Sensing Letters*, vol. 11, no. 5, pp. 930–934, 2013.
- [5] G. Vivone, R. Restaino, and J. Chanussot, “A regression-based high-pass modulation pansharpening approach,” *IEEE Transactions on geoscience and remote sensing*, vol. 56, no. 2, pp. 984–996, 2017.

- [6] B. Aiazzi, L. Alparone, S. Baronti, A. Garzelli, and M. Selva, "Mtf-tailored multiscale fusion of high-resolution ms and pan imagery," *Photogrammetric Engineering & Remote Sensing*, vol. 72, no. 5, pp. 591–596, 2006.
- [7] G. Vivone, R. Restaino, and J. Chanussot, "Full scale regression-based injection coefficients for panchromatic sharpening," *IEEE Transactions on Image Processing*, vol. 27, no. 7, pp. 3418–3431, 2018.
- [8] W. Carper, T. Lillesand, R. Kiefer *et al.*, "The use of intensity-hue-saturation transformations for merging spot panchromatic and multispectral image data," *Photogrammetric Engineering and remote sensing*, vol. 56, no. 4, pp. 459–467, 1990.
- [9] P. Kwarteng and A. Chavez, "Extracting spectral contrast in landsat thematic mapper image data using selective principal component analysis," *Photogramm. Eng. Remote Sens.*, vol. 55, no. 1, pp. 339–348, 1989.
- [10] C. A. Laben and B. V. Brower, "Process for enhancing the spatial resolution of multispectral imagery using pan-sharpening," Jan. 4 2000, uS Patent 6,011,875.
- [11] B. Aiazzi, S. Baronti, and M. Selva, "Improving component substitution pansharpening through multivariate regression of ms + pan data," *IEEE Transactions on Geoscience and Remote Sensing*, vol. 45, no. 10, pp. 3230–3239, 2007.
- [12] R. Restaino, M. Dalla Mura, G. Vivone, and J. Chanussot, "Context-adaptive pansharpening based on image segmentation," *IEEE Transactions on Geoscience and Remote Sensing*, vol. 55, no. 2, pp. 753–766, 2016.
- [13] S. Lolli, L. Alparone, A. Garzelli, and G. Vivone, "Haze correction for contrast-based multispectral pansharpening," *IEEE Geoscience and Remote Sensing Letters*, vol. 14, no. 12, pp. 2255–2259, 2017.
- [14] A. R. Gillespie, A. B. Kahle, and R. E. Walker, "Color enhancement of highly correlated images. ii. channel ratio and "chromaticity" transformation techniques," *Remote Sensing of Environment*, vol. 22, no. 3, pp. 343–365, 1987.
- [15] G. Vivone, "Robust band-dependent spatial-detail approaches for panchromatic sharpening," *IEEE transactions on Geoscience and Remote Sensing*, vol. 57, no. 9, pp. 6421–6433, 2019.
- [16] M. R. Vicinanza, R. Restaino, G. Vivone, M. Dalla Mura, and J. Chanussot, "A pansharpening method based on the sparse representation of injected details," *IEEE Geoscience and Remote Sensing Letters*, vol. 12, no. 1, pp. 180–184, 2014.
- [17] F. Palsson, J. R. Sveinsson, and M. O. Ulfarsson, "A new pansharpening algorithm based on total variation," *IEEE Geoscience and Remote Sensing Letters*, vol. 11, no. 1, pp. 318–322, 2013.
- [18] W. Huang, L. Xiao, Z. Wei, H. Liu, and S. Tang, "A new pan-sharpening method with deep neural networks," *IEEE Geoscience and Remote Sensing Letters*, vol. 12, no. 5, pp. 1037–1041, 2015.
- [19] G. Masi, D. Cozzolino, L. Verdoliva, and G. Scarpa, "Pansharpening by convolutional neural networks," *Remote Sensing*, vol. 8, no. 7, p. 594, 2016.
- [20] J. Zhong, B. Yang, G. Huang, F. Zhong, and Z. Chen, "Remote sensing image fusion with convolutional neural network," *Sensing and Imaging*, vol. 17, pp. 1–16, 2016.
- [21] G. Yang, X. Cao, W. Xiao, M. Zhou, A. Liu, D. Meng *et al.*, "Panflownet: A flow-based deep network for pan-sharpening," *arXiv preprint arXiv:2305.07774*, 2023.
- [22] X. Cao, Y. Chen, and W. Cao, "Proximal pannet: A model-based deep network for pansharpening," in *Proceedings of the AAAI Conference on Artificial Intelligence*, vol. 36, no. 1, 2022, pp. 176–184.
- [23] X. Fu, M. Wang, X. Cao, X. Ding, and Z.-J. Zha, "A model-driven deep unfolding method for jpeg artifacts removal," *IEEE Transactions on Neural Networks and Learning Systems*, vol. 33, no. 11, pp. 6802–6816, 2021.
- [24] Q. Xie, M. Zhou, Q. Zhao, D. Meng, W. Zuo, and Z. Xu, "Multispectral and hyperspectral image fusion by ms/hs fusion net," in *Proceedings of the IEEE/CVF Conference on Computer Vision and Pattern Recognition*, 2019, pp. 1585–1594.
- [25] Y. Wei, Q. Yuan, H. Shen, and L. Zhang, "Boosting the accuracy of multispectral image pansharpening by learning a deep residual network," *IEEE Geoscience and Remote Sensing Letters*, vol. 14, no. 10, pp. 1795–1799, 2017.
- [26] Q. Yuan, Y. Wei, X. Meng, H. Shen, and L. Zhang, "A multiscale and multidepth convolutional neural network for remote sensing imagery pan-sharpening," *IEEE Journal of Selected Topics in Applied Earth Observations and Remote Sensing*, vol. 11, no. 3, pp. 978–989, 2018.
- [27] L. He, Y. Rao, J. Li, J. Chanussot, A. Plaza, J. Zhu, and B. Li, "Pansharpening via detail injection based convolutional neural networks," *IEEE Journal of Selected Topics in Applied Earth Observations and Remote Sensing*, vol. 12, no. 4, pp. 1188–1204, 2019.
- [28] Y. Zhang, C. Liu, M. Sun, and Y. Ou, "Pan-sharpening using an efficient bidirectional pyramid network," *IEEE Transactions on Geoscience and Remote Sensing*, vol. 57, no. 8, pp. 5549–5563, 2019.
- [29] G. Scarpa, S. Vitale, and D. Cozzolino, "Target-adaptive cnn-based pansharpening," *IEEE Transactions on Geoscience and Remote Sensing*, vol. 56, no. 9, pp. 5443–5457, 2018.
- [30] L.-J. Deng, G. Vivone, C. Jin, and J. Chanussot, "Detail injection-based deep convolutional neural networks for pansharpening," *IEEE Transactions on Geoscience and Remote Sensing*, vol. 59, no. 8, pp. 6995–7010, 2020.
- [31] G. Yang, M. Zhou, K. Yan, A. Liu, X. Fu, and F. Wang, "Memory-augmented deep conditional unfolding network for pan-sharpening," in *Proceedings of the IEEE/CVF conference on computer vision and pattern recognition*, 2022, pp. 1788–1797.
- [32] M. Zhou, J. Huang, Y. Fang, X. Fu, and A. Liu, "Pan-sharpening with customized transformer and invertible neural network," in *Proceedings of the AAAI conference on artificial intelligence*, vol. 36, no. 3, 2022, pp. 3553–3561.
- [33] K. Zhang, A. Wang, F. Zhang, W. Wan, J. Sun, and L. Bruzzone, "Spatial-spectral dual back-projection network for pansharpening," *IEEE Transactions on Geoscience and Remote Sensing*, vol. 61, pp. 1–16, 2023.
- [34] X. Meng, H. Shen, H. Li, L. Zhang, and R. Fu, "Review of the pansharpening methods for remote sensing images based on the idea of meta-analysis: Practical discussion and challenges," *Information Fusion*, vol. 46, pp. 102–113, 2019.
- [35] A. Ben-Israel and T. N. Greville, *Generalized inverses: theory and applications*. Springer Science & Business Media, 2003, vol. 15.
- [36] C. Radhakrishna Rao, "Calculus of generalized inverses of matrices part i. general theory," *Sankhya-Series A*, vol. 29, pp. 317–342, 1967.
- [37] M. Planitz, "3. inconsistent systems of linear equations," *The Mathematical Gazette*, vol. 63, no. 425, pp. 181–185, 1979.
- [38] J. Ho, A. Jain, and P. Abbeel, "Denoising diffusion probabilistic models," *Advances in neural information processing systems*, vol. 33, pp. 6840–6851, 2020.
- [39] B. Poole, A. Jain, J. T. Barron, and B. Mildenhall, "Dreamfusion: Text-to-3d using 2d diffusion," *arXiv preprint arXiv:2209.14988*, 2022.
- [40] G. Vivone, M. Dalla Mura, A. Garzelli, and F. Pacifici, "A benchmarking protocol for pansharpening: Dataset, preprocessing, and quality assessment," *IEEE Journal of Selected Topics in Applied Earth Observations and Remote Sensing*, vol. 14, pp. 6102–6118, 2021.
- [41] A. Hore and D. Ziou, "Image quality metrics: Psnr vs. ssim," in *2010 20th international conference on pattern recognition*. IEEE, 2010, pp. 2366–2369.
- [42] L.-J. Deng, G. Vivone, M. E. Paoletti, G. Scarpa, J. He, Y. Zhang, J. Chanussot, and A. Plaza, "Machine learning in pansharpening: A benchmark, from shallow to deep networks," *IEEE Geoscience and Remote Sensing Magazine*, vol. 10, no. 3, pp. 279–315, 2022.
- [43] N. Yokoya and A. Iwasaki, "Airborne hyperspectral data over chikusei," *Space Appl. Lab., Univ. Tokyo, Tokyo, Japan, Tech. Rep. SAL-2016-05-27*, vol. 5, p. 5, 2016.
- [44] P. Dhariwal and A. Nichol, "Diffusion models beat gans on image synthesis," *Advances in neural information processing systems*, vol. 34, pp. 8780–8794, 2021.
- [45] G. Vivone, M. Dalla Mura, A. Garzelli, R. Restaino, G. Scarpa, M. O. Ulfarsson, L. Alparone, and J. Chanussot, "A new benchmark based on recent advances in multispectral pansharpening: Revisiting pansharpening with classical and emerging pansharpening methods," *IEEE Geoscience and Remote Sensing Magazine*, vol. 9, no. 1, pp. 53–81, 2020.
- [46] Z. Wang, D. Ziou, C. Armenakis, D. Li, and Q. Li, "A comparative analysis of image fusion methods," *IEEE transactions on geoscience and remote sensing*, vol. 43, no. 6, pp. 1391–1402, 2005.
- [47] L. Alparone, L. Wald, J. Chanussot, C. Thomas, P. Gamba, and L. M. Bruce, "Comparison of pansharpening algorithms: Outcome of the 2006 grs-s data-fusion contest," *IEEE Transactions on Geoscience and Remote Sensing*, vol. 45, no. 10, pp. 3012–3021, 2007.
- [48] D. P. Kingma and J. Ba, "Adam: A method for stochastic optimization," *arXiv preprint arXiv:1412.6980*, 2014.
- [49] J. Yang, X. Fu, Y. Hu, Y. Huang, X. Ding, and J. Paisley, "Pannet: A deep network architecture for pan-sharpening," in *Proceedings of the IEEE international conference on computer vision*, 2017, pp. 5449–5457.
- [50] J. Deng, W. Dong, R. Socher, L.-J. Li, K. Li, and L. Fei-Fei, "Imagenet: A large-scale hierarchical image database," in *2009 IEEE conference on computer vision and pattern recognition*. Ieee, 2009, pp. 248–255.

## APPENDIX

## A. Proofs

**Theorem II.4** We can use linear equations to rewrite the  $\mathbf{BY} - \mathbf{ZA}$  in Kronecker form, i.e,

$$[\mathbf{Z}_{hw \times S} \otimes \mathbf{I}_{s \times s}, -\mathbf{I}_{hw \times hw} \otimes \mathbf{Y}_{s \times HW}^T] \begin{bmatrix} \text{vec}(\mathbf{A}) \\ \text{vec}(\mathbf{B}) \end{bmatrix}_{Ss + hwHW} = 0, \quad (28)$$

where the Kronecker product  $\mathbf{Z} \otimes \mathbf{I} = \begin{bmatrix} z_{1,1}\mathbf{I} & z_{1,2}\mathbf{I} & \cdots & z_{1,S}\mathbf{I} \\ z_{2,1}\mathbf{I} & z_{2,2}\mathbf{I} & \cdots & z_{2,S}\mathbf{I} \\ \vdots & \vdots & \ddots & \vdots \\ z_{hw,1}\mathbf{I} & z_{hw,2}\mathbf{I} & \cdots & z_{hw,S}\mathbf{I} \end{bmatrix}$  and  $\text{vec}(\mathbf{A}) = [a_{11}, \dots, a_{S1}, a_{12}, \dots, a_{S2}, \dots, a_{1s}, \dots, a_{Ss}]^T$ .

$\mathbf{BY} = \mathbf{ZA}$  has a nonzero solution for  $\mathbf{B}$  and  $\mathbf{A}$

$\Leftrightarrow$

- $(HW \geq s)$  or  $(HW < s \text{ and } hw < \frac{Ss}{s-HW})$
- $(HW < s \text{ and } hw \geq \frac{Ss}{s-HW})$  and  $\text{rank}([\mathbf{Z}_{hw \times S} \otimes \mathbf{I}_{s \times s}, -\mathbf{I}_{hw \times hw} \otimes \mathbf{Y}_{s \times HW}^T]) < \min(hws, Ss + hwHW)$ .

*Proof.* Let  $\mathbf{M} = [\mathbf{Z}_{hw \times S} \otimes \mathbf{I}_{s \times s}, -\mathbf{I}_{hw \times hw} \otimes \mathbf{Y}_{s \times HW}^T]$  and  $\mathbf{x} = \begin{bmatrix} \text{vec}(\mathbf{A}) \\ \text{vec}(\mathbf{B}) \end{bmatrix}_{Ss + hwHW}$ . It yields

$\mathbf{Mx} = 0$  has non-zero solution

$\Leftrightarrow$

- $hws < Ss + hwHW$
- $(hws \geq Ss + hwHW \text{ and } \text{rank}(\mathbf{M}) < \min(hws, Ss + hwHW))$

$\Leftrightarrow$

- $(HW \geq s)$  or  $(HW < s \text{ and } hw < \frac{Ss}{s-HW})$
- $(HW < s \text{ and } hw \geq \frac{Ss}{s-HW})$  and  $\text{rank}(\mathbf{M}) < \min(hws, Ss + hwHW)$ .

□

**Theorem II.5.** if the matrix equations in **Assumption II.1** have a solution, then one solution format to the **Assumption II.1** is the following

$$\mathbf{X}_{mra} = \mathbf{B}^{-} \mathbf{Z} + (\mathbf{I} - \mathbf{B}^{-} \mathbf{B}) \mathbf{Y} \mathbf{A}^{-}, \quad (29)$$

According to [35], the general solution space is

$$\mathbf{X} = \mathbf{X}_{mra} + (\mathbf{I} - \mathbf{B}^{-} \mathbf{B}) \mathbf{W} (\mathbf{I} - \mathbf{A} \mathbf{A}^{-}), \quad (30)$$

where  $\mathbf{W} \in R^{HW \times S}$  is an arbitrary matrix.

*Proof.* "⇒"  $\forall \mathbf{W} \in R^{HW \times S}, \mathbf{A}^{-} \in \mathbf{A}\{-\}, \mathbf{B}^{-} \in \mathbf{B}\{-\}$ , according to Theorem II.3,

$$\mathbf{BY} = \mathbf{ZA} \quad (31)$$

$$\mathbf{Y} = \mathbf{YA}^{-} \mathbf{A} \quad (32)$$

$$\mathbf{Z} = \mathbf{BB}^{-} \mathbf{Z}, \quad (33)$$

we have

$$\begin{aligned} \mathbf{BX} &= \mathbf{B}(\mathbf{X}_{mra} + (\mathbf{I} - \mathbf{B}^{-} \mathbf{B}) \mathbf{W} (\mathbf{I} - \mathbf{A} \mathbf{A}^{-})) \\ &= \mathbf{BX}_{mra} \\ &= \mathbf{B}(\mathbf{B}^{-} \mathbf{Z} + (\mathbf{I} - \mathbf{B}^{-} \mathbf{B}) \mathbf{Y} \mathbf{A}^{-}) \\ &= \mathbf{BB}^{-} \mathbf{Z} \\ &= \mathbf{Z}, \end{aligned} \quad (34)$$

$$\begin{aligned} \mathbf{XA} &= (\mathbf{X}_{mra} + (\mathbf{I} - \mathbf{B}^{-} \mathbf{B}) \mathbf{W} (\mathbf{I} - \mathbf{A} \mathbf{A}^{-})) \mathbf{A} \\ &= \mathbf{X}_{mra} \mathbf{A} \\ &= (\mathbf{B}^{-} \mathbf{Z} + (\mathbf{I} - \mathbf{B}^{-} \mathbf{B}) \mathbf{Y} \mathbf{A}^{-}) \mathbf{A} \\ &= \mathbf{B}^{-} \mathbf{ZA} + \mathbf{YA}^{-} \mathbf{A} - \mathbf{B}^{-} \mathbf{BYA}^{-} \mathbf{A} \\ &= \mathbf{B}^{-} \mathbf{ZA} + \mathbf{YA}^{-} \mathbf{A} - \mathbf{B}^{-} \mathbf{ZAA}^{-} \mathbf{A} \\ &= \mathbf{YA}^{-} \mathbf{A} \\ &= \mathbf{Y}. \end{aligned} \quad (35)$$

” $\Leftarrow$ ”  $\forall \mathbf{X}$ , take  $\mathbf{W} = \mathbf{X} - \mathbf{X}_{mra}$ , it yields

$$\begin{aligned}
 & \mathbf{X} - (\mathbf{X}_{mra} + (\mathbf{I} - \mathbf{B}^\top \mathbf{B})(\mathbf{X} - \mathbf{X}_{mra})(\mathbf{I} - \mathbf{A}\mathbf{A}^\top)) \\
 &= \mathbf{X} - \mathbf{X}_{mra} - (\mathbf{I} - \mathbf{B}^\top \mathbf{B})(\mathbf{X} - \mathbf{X}_{mra})(\mathbf{I} - \mathbf{A}\mathbf{A}^\top) \\
 &= \mathbf{B}^\top \mathbf{B}(\mathbf{X} - \mathbf{X}_{mra}) + (\mathbf{X} - \mathbf{X}_{mra})\mathbf{A}\mathbf{A}^\top - \mathbf{B}^\top \mathbf{B}(\mathbf{X} - \mathbf{X}_{mra})\mathbf{A}\mathbf{A}^\top \\
 &= \mathbf{B}^\top(\mathbf{Y} - \mathbf{Y}) + (\mathbf{Z} - \mathbf{Z})\mathbf{A}^\top - \mathbf{B}^\top(\mathbf{Y} - \mathbf{Y})\mathbf{A}\mathbf{A}^\top \\
 &= 0.
 \end{aligned} \tag{36}$$

□

**Theorem II.6.** If the matrix equations in **Assumption II.1** have a solution, then one solution format to the **Assumption II.1** is the following

$$\mathbf{X}_{cs} = \mathbf{B}^\top \mathbf{Z} + (\mathbf{Y} - \mathbf{B}^\top \mathbf{Z}\mathbf{A})\mathbf{A}^\top, \tag{37}$$

and the general solution space is

$$\mathbf{X} = \mathbf{X}_{cs} + (\mathbf{I} - \mathbf{B}^\top \mathbf{B})\mathbf{W}(\mathbf{I} - \mathbf{A}\mathbf{A}^\top), \tag{38}$$

where  $\mathbf{W} \in R^{HW \times S}$  is an arbitrary matrix.

*Proof.* ” $\Rightarrow$ ”  $\forall \mathbf{W} \in R^{HW \times S}, \mathbf{A}^\top \in \mathbf{A}\{-\}, \mathbf{B}^\top \in \mathbf{B}\{-\}$ , since the matrix equations in **Assumption II.1** have a solution, according to Theorem II.3,

$$\mathbf{B}\mathbf{Y} = \mathbf{Z}\mathbf{A} \tag{39}$$

$$\mathbf{Y} = \mathbf{Y}\mathbf{A}^\top \mathbf{A} \tag{40}$$

$$\mathbf{Z} = \mathbf{B}\mathbf{B}^\top \mathbf{Z}, \tag{41}$$

we have

$$\mathbf{X}_{cs} = \mathbf{B}^\top \mathbf{Z} + (\mathbf{Y} - \mathbf{B}^\top \mathbf{Z}\mathbf{A})\mathbf{A}^\top = \mathbf{Y}\mathbf{A}^\top + \mathbf{B}^\top \mathbf{Z}(\mathbf{I} - \mathbf{A}\mathbf{A}^\top). \tag{42}$$

It yields

$$\begin{aligned}
 \mathbf{X}\mathbf{A} &= (\mathbf{X}_{cs} + (\mathbf{I} - \mathbf{B}^\top \mathbf{B})\mathbf{W}(\mathbf{I} - \mathbf{A}\mathbf{A}^\top))\mathbf{A} \\
 &= (\mathbf{Y}\mathbf{A}^\top + \mathbf{B}^\top \mathbf{Z}(\mathbf{I} - \mathbf{A}\mathbf{A}^\top))\mathbf{A}^\top \\
 &= \mathbf{Y}\mathbf{A}^\top \mathbf{A} \\
 &= \mathbf{Y},
 \end{aligned} \tag{43}$$

$$\begin{aligned}
 \mathbf{B}\mathbf{X} &= \mathbf{B}(\mathbf{X}_{cs} + (\mathbf{I} - \mathbf{B}^\top \mathbf{B})\mathbf{W}(\mathbf{I} - \mathbf{A}\mathbf{A}^\top)) \\
 &= \mathbf{B}(\mathbf{Y}\mathbf{A}^\top + \mathbf{B}^\top \mathbf{Z}(\mathbf{I} - \mathbf{A}\mathbf{A}^\top)) \\
 &= \mathbf{Z}\mathbf{A}\mathbf{A}^\top + \mathbf{B}\mathbf{B}^\top \mathbf{Z}(\mathbf{I} - \mathbf{A}\mathbf{A}^\top) \\
 &= \mathbf{Z}\mathbf{A}\mathbf{A}^\top + \mathbf{Z}(\mathbf{I} - \mathbf{A}\mathbf{A}^\top) \\
 &= \mathbf{Z}.
 \end{aligned} \tag{44}$$

” $\Leftarrow$ ”  $\forall \mathbf{X}$  satisfying **Assumption II.1**, take  $\mathbf{W} = \mathbf{X} - \mathbf{X}_{cs}$ , it yields

$$\begin{aligned}
 & \mathbf{X} - (\mathbf{X}_{cs} + (\mathbf{I} - \mathbf{B}^\top \mathbf{B})(\mathbf{X} - \mathbf{X}_{cs})(\mathbf{I} - \mathbf{A}\mathbf{A}^\top)) \\
 &= \mathbf{X} - \mathbf{X}_{cs} - (\mathbf{I} - \mathbf{B}^\top \mathbf{B})(\mathbf{X} - \mathbf{X}_{cs})(\mathbf{I} - \mathbf{A}\mathbf{A}^\top) \\
 &= \mathbf{B}^\top \mathbf{B}(\mathbf{X} - \mathbf{X}_{cs}) + (\mathbf{X} - \mathbf{X}_{cs})\mathbf{A}\mathbf{A}^\top - \mathbf{B}^\top \mathbf{B}(\mathbf{X} - \mathbf{X}_{cs})\mathbf{A}\mathbf{A}^\top \\
 &= \mathbf{B}^\top(\mathbf{Y} - \mathbf{Y}) + (\mathbf{Z} - \mathbf{Z})\mathbf{A}^\top - \mathbf{B}^\top(\mathbf{Y} - \mathbf{Y})\mathbf{A}\mathbf{A}^\top \\
 &= 0.
 \end{aligned} \tag{45}$$

□

**Theorem II.7** If the matrix equation in **Assumption II.1** has a solution, for fixed  $\mathbf{A}^\top \in \mathbf{A}\{-\}$  and  $\mathbf{B}^\top \in \mathbf{B}\{-\}$  then  $\mathbf{X}_{cs} = \mathbf{X}_{mra}$ .

*Proof.* Since  $\mathbf{Z}\mathbf{A} = \mathbf{B}\mathbf{Y}$ ,

$$\mathbf{X}_{cs} = \mathbf{B}^\top \mathbf{Z} + (\mathbf{Y} - \mathbf{B}^\top \mathbf{Z}\mathbf{A})\mathbf{A}^\top = \mathbf{B}^\top \mathbf{Z} + (\mathbf{Y} - \mathbf{B}^\top \mathbf{B}\mathbf{Y})\mathbf{A}^\top = \mathbf{X}_{mra}. \tag{46}$$

□

**Theorem II.8** The Gram Schmidt adaptive method can be described as follows: Suppose  $\text{var}(\mathbf{ZA})$  is invertible. Define

$$\mathbf{W} = \text{var}(\mathbf{ZA})^{-1} \text{cov}(\mathbf{ZA}, \mathbf{Z}) \in \mathbf{A}\{-\} \quad (47)$$

where

$$\text{cov}(\mathbf{ZA}, \mathbf{Z}) = \frac{1}{hw} (\mathbf{ZA} - \mathbf{1} \frac{\mathbf{1}^T}{hw} \mathbf{ZA})^T (\mathbf{Z} - \mathbf{1} \frac{\mathbf{1}^T}{hw} \mathbf{Z}), \quad (48)$$

$$\text{var}(\mathbf{ZA}) = \frac{1}{hw} (\mathbf{ZA} - \mathbf{1} \frac{\mathbf{1}^T}{hw} \mathbf{ZA})^T (\mathbf{ZA} - \mathbf{1} \frac{\mathbf{1}^T}{hw} \mathbf{ZA}), \quad (49)$$

It yields

$$\mathbf{X}_{gsa} = \mathbf{B}^{-} \mathbf{Z} + (\mathbf{Y} - \mathbf{B}^{-} \mathbf{ZA}) \mathbf{W}. \quad (50)$$

The Gram Schmidt adaptive method can be viewed as a special case of the representation in the Theorem II.6. It yields

$$\mathbf{Y} = \mathbf{X}_{gsa} \mathbf{A} \quad (51)$$

$$\mathbf{Z} = \mathbf{B} \mathbf{X}_{gsa}. \quad (52)$$

*Proof.* According to the format of Equation 50, we only need to show that  $W$  is the generalized inverse of  $A$  that is  $AWA = A$ . Here, we only need to show that  $WA = 1$ .

$$\text{cov}(\mathbf{ZA}, \mathbf{Z}) \mathbf{A} = \frac{1}{hw} (\mathbf{ZA} - \mathbf{1} \frac{\mathbf{1}^T}{hw} \mathbf{ZA})^T (\mathbf{Z} - \mathbf{1} \frac{\mathbf{1}^T}{hw} \mathbf{Z}) \mathbf{A} = \text{var}(\mathbf{ZA}), \quad (53)$$

it yields

$$\mathbf{WA} = \text{var}(\mathbf{ZA})^{-1} \text{var}(\mathbf{ZA}) = \mathbf{I}. \quad (54)$$

Therefore,  $X_{gsa}$  satisfies

$$\mathbf{Y} = \mathbf{X}_{gsa} \mathbf{A} \quad (55)$$

$$\mathbf{Z} = \mathbf{B} \mathbf{X}_{gsa}. \quad (56)$$

□

**Theorem II.9** If  $\mathbf{X}_{recover} = \mathbf{VZ} + (\mathbf{Y} - \mathbf{VZA}) \mathbf{W}$ , then  $\mathbf{X}_{recover} \mathbf{A} - \mathbf{Y} = (\mathbf{I} - \mathbf{WA})(\mathbf{VZA} - \mathbf{Y})$ .

*Proof.*

$$\begin{aligned} \mathbf{X}_{recover} \mathbf{A} - \mathbf{Y} &= (\mathbf{VZA} + (\mathbf{Y} - \mathbf{VZA}) \mathbf{W}) \mathbf{A} - \mathbf{Y} \\ &= (\mathbf{VZA} + \mathbf{YWA} - \mathbf{VZAWA}) - \mathbf{Y} \\ &= (\mathbf{VZA} - \mathbf{Y})(\mathbf{I} - \mathbf{WA}). \end{aligned} \quad (57)$$

□

**Theorem II.10** If  $\mathbf{X}_{recover} = \mathbf{VZA} + (\mathbf{Y} - \mathbf{VZA}) \mathbf{W}$ , then  $\mathbf{B} \mathbf{X}_{recover} - \mathbf{Z} = \mathbf{BVZ} - \mathbf{Z} + \mathbf{B}(\mathbf{Y} - \mathbf{VZA}) \mathbf{W}$ .

*Proof.*

$$\begin{aligned} \mathbf{B} \mathbf{X}_{recover} - \mathbf{Z} &= \mathbf{B}(\mathbf{VZ} + (\mathbf{Y} - \mathbf{VZA}) \mathbf{W}) - \mathbf{Z} \\ &= \mathbf{BVZ} + \mathbf{BYW} - \mathbf{BVZAW} - \mathbf{Z} \\ &= \mathbf{BVZ} - \mathbf{Z} + \mathbf{B}(\mathbf{Y} - \mathbf{VZA}) \mathbf{W} \end{aligned} \quad (58)$$

□

**Theorem II.11** If  $\mathbf{X}_{recover} = \mathbf{VZA} + (\mathbf{Y} - \mathbf{VBY}) \mathbf{W}$ , then  $\mathbf{X}_{recover} \mathbf{A} - \mathbf{Y} = \mathbf{V}(\mathbf{ZA} - \mathbf{BY}) - (\mathbf{I} - \mathbf{VB}) \mathbf{Y}(\mathbf{I} - \mathbf{WA})$ .

*Proof.*

$$\begin{aligned} \mathbf{X}_{recover} \mathbf{A} - \mathbf{Y} &= (\mathbf{VZA} + (\mathbf{Y} - \mathbf{VBY}) \mathbf{W}) \mathbf{A} - \mathbf{Y} \\ &= (\mathbf{VBY} + \mathbf{V}(\mathbf{ZA} - \mathbf{BY}) + \mathbf{YWA} - \mathbf{Y} - \mathbf{VBYWA}) \\ &= \mathbf{V}(\mathbf{ZA} - \mathbf{BY}) - (\mathbf{I} - \mathbf{VB}) \mathbf{Y}(\mathbf{I} - \mathbf{WA}). \end{aligned} \quad (59)$$

□

**Theorem II.12** If  $\mathbf{X}_{recover} = \mathbf{VZA} + (\mathbf{Y} - \mathbf{VBY}) \mathbf{W}$ , then  $\mathbf{B} \mathbf{X}_{recover} - \mathbf{Z} = (\mathbf{BV} - \mathbf{I}) \mathbf{Z} + (\mathbf{B} - \mathbf{BVB}) \mathbf{YW}$ .

*Proof.*

$$\begin{aligned}
 \mathbf{B}\mathbf{X}_{recover} - \mathbf{Z} &= \mathbf{B}(\mathbf{V}\mathbf{Z} + (\mathbf{Y} - \mathbf{V}\mathbf{B}\mathbf{Y})\mathbf{W}) - \mathbf{Z} \\
 &= \mathbf{BVZ} + \mathbf{BYW} - \mathbf{BVBYW} - \mathbf{Z} \\
 &= \mathbf{BVZ} - \mathbf{Z} + \mathbf{BYW} - \mathbf{BVBYW} \\
 &= (\mathbf{BV} - \mathbf{I})\mathbf{Z} + (\mathbf{B} - \mathbf{B}\mathbf{V}\mathbf{B})\mathbf{YW}
 \end{aligned} \tag{60}$$

□

**Theorem II.13** With down-sampling enhancement(DSE), the prior component substitution method and prior multiresolution analysis methods are equivalent. That is If  $\mathbf{B} = \mathbf{ZZ}^+\hat{\mathbf{B}}$  and  $\mathbf{A} = \mathbf{Z}^+\hat{\mathbf{B}}\mathbf{Y}$ , then  $\mathbf{X}_{mra} = \mathbf{B}^-\mathbf{Z} + (\mathbf{I} - \mathbf{B}^-\mathbf{B})\mathbf{YW} = \mathbf{X}_{cs} = \mathbf{B}^-\mathbf{Z} + (\mathbf{Y} - \mathbf{B}^-\mathbf{ZA})\mathbf{W}$ .

*Proof.* We only need to prove  $\mathbf{B}^-\mathbf{BYW} = \mathbf{BZA}\mathbf{W}$ . Since with down-sampling enhancement,  $\mathbf{B} = \mathbf{ZZ}^+\hat{\mathbf{B}}$  and  $\mathbf{A} = \mathbf{Z}^+\hat{\mathbf{B}}\mathbf{Y}$ , we have

$$\mathbf{B}^-\mathbf{BYW} = \mathbf{B}^-\mathbf{ZZ}^+\hat{\mathbf{B}}\mathbf{YW} = \mathbf{BZA}\mathbf{W}.$$

□

**Theorem II.14** If the Assumption II.1 has a solution, then the ground truth  $\mathbf{X}$  and  $\mathbf{X}_{mra}$  is different in the following,

$$\mathbf{X} - \mathbf{X}_{mra} = (\mathbf{I} - \mathbf{B}^-\mathbf{B})\mathbf{X}(\mathbf{I} - \mathbf{AA}^-). \tag{61}$$

*Proof.*

$$\begin{aligned}
 \mathbf{X} - (\mathbf{B}^-\mathbf{Z} + (\mathbf{Y} - \mathbf{B}^-\mathbf{BY})\mathbf{A}^-) &= \mathbf{X} - (\mathbf{B}^-\mathbf{BX} + (\mathbf{XA} - \mathbf{B}^-\mathbf{BX}\mathbf{A})\mathbf{A}^-) \\
 &= (\mathbf{I} - \mathbf{B}^-\mathbf{B})\mathbf{X} + (\mathbf{I} - \mathbf{BB}^-)\mathbf{XA}\mathbf{A}^- \\
 &= (\mathbf{I} - \mathbf{B}^-\mathbf{B})\mathbf{X}(\mathbf{I} - \mathbf{AA}^-)
 \end{aligned} \tag{62}$$

□

## B. Detailed dataset descriptions for Chikusei dataset and PAirMax dataset

**Detailed dataset description for the Chikusei dataset.** [43] This airborne hyperspectral dataset, acquired by a Headwall Hyperspec-VNIR-C sensor over Chikusei, Ibaraki, Japan, on July 29, 2014 (9:56-10:53 UTC+9), features 128 bands covering 363 nm to 1018 nm. The scene (center: 36.294946°N, 140.008380°E) covers agricultural and urban areas with dimensions of 2517x2335 pixels and a 2.5 m ground sampling distance. Field surveys and visual interpretation of high-resolution Canon EOS 5D Mark II images collected alongside the flight provided ground truth labels for 19 classes(not used). The dataset and ground truth are distributed in ENVI and MATLAB formats for scientific use.

**Detailed dataset description for the PAirMax dataset.** [40] The PAirMax dataset consists of 14 scenes selected as representative examples of the heterogeneity encountered in Pan-sharpening applications. The dataset includes 14 Full-Resolution (FR) datasets. 14 Reduced-Resolution (RR) datasets were generated from these FR test cases. Most images depict urban areas, presenting significant pansharpening challenges such as accurately rendering high-contrast features (e.g., building edges), sub-resolution details, and avoiding spectral smearing across adjacent regions with differing spectral properties. Some scenes feature natural land cover types, including vegetation (agricultural fields, meadows, forests), and water bodies. Vegetated areas pose challenges due to the distinct reflectance difference between visible and NIR wavelengths (caused by chlorophyll) and textured patterns with sub-pixel size, potentially leading to spectral and spatial distortions. Water regions are included to assess spectral reconstruction, particularly relevant for sensors with bathymetry-optimized bands (e.g., WorldView-2/3), and often feature sharp edges against urban embankments. The scenes were acquired across different seasons, introducing variations in illumination conditions, such as dimmer intensities and elongated shadows in winter imagery. All PAN-MS bundles exhibit a spatial resolution ratio of 4:1 (PAN has 16 times more pixels than each MS band). MS bands cover the Visible and Near-Infrared (VNIR) domain, with either four bands (GeoEye-1, WorldView-2, SPOT-7) or eight bands (WorldView-2/3). The 14 images in PAirMax were derived from original PAN+MS bundles acquired under clear-sky conditions with negligible cloud cover (especially within the selected cropped areas).



Fig. 6: Synthetic PAN and HS images. RGB represents the red green blue channel and OAP represents the other selected three channels.

TABLE V: Reduced-resolution comparative experiments on WV3 New York Dataset

Method	Q2n( $\uparrow$ )	SAM( $\downarrow$ )	ERGAS( $\downarrow$ )
GT	1.0000	0.0000	0.0000
EXP	0.6555	7.2344	8.2676
BT-H	0.9261	6.4689	3.9948
BDSD-PC	0.9334	6.8699	3.9157
C-GSA	0.9235	6.7104	4.0751
SR-D	0.9098	6.6782	4.4543
MTF-GLP-HPM-R	0.9245	7.0266	4.0949
MTF-GLP-FS	0.9246	6.7789	4.0691
TV	0.9294	6.6165	4.0824
PanNet	0.9217	6.9522	4.3506
DRPNN	0.9224	7.4331	4.2887
MSDCNN	0.9093	7.5705	4.4867
BDPN	0.9198	7.7437	4.4823
DiCNN	0.8558	8.1309	5.6302
PNN	0.8830	12.6763	6.8061
APNN	0.9119	7.6778	4.5471
FusionNet	0.8534	8.4185	6.1608
PCS/PMRA	0.8703	9.9481	5.6316

### C. Synthetic PAN and HS images in synthetic experiments.

### D. Down-sampling and up-sampling parameters illustration

In the comparative experiment, we use bilinear down-sampling and bilinear up-sampling. In the synthetic experiment, we use mean down-sampling to create the data and use bilinear down-sampling and bilinear up-sampling for calculation of our method. In ablation study and diffusion-related experiment, we use mean down-sampling and nearest neighborhood up-sampling.

### E. Reduced-resolution comparative experiments

In the reduced-resolution comparative experiments, our method does not perform outstandingly because it has not been refined by searching the general solution space with the diffusion prior.